JOURNAL OF PETROLOGY

Journal of Petrology, 2016, Vol. 57, No. 4, 685–715
doi: 10.1093/petrology/egv048
Advance Access Publication Date: 9 October 2015
Original Article

OXFORD

Geochemical and Os–Hf–Nd–Sr Isotopic Characterization of North Patagonian Mantle Xenoliths: Implications for Extensive Melt Extraction and Percolation Processes

A. Mundl[1]*, T. Ntaflos[1], L. Ackerman[2,3], M. Bizimis[4], E. A. Bjerg[5], W. Wegner[1] and C. A. Hauzenberger[6]

[1]Department of Lithospheric Research, University of Vienna, Althanstrasse 14, 1090 Vienna, Austria, [2]Institute of Geology v.v.i., Academy of Sciences of the Czech Republic, Rozvojová 269, 165 00 Prague 6—Lysolaje, Czech Republic, [3]Czech Geological Survey, Geologická 6, 152 00 Prague 5, Czech Republic, [4]Department of Earth and Ocean Sciences, University of South Carolina, 701 Sumter Street, Columbia, SC 29208, USA, [5]INGEOSUR (CONICET-UNS) and Departamento de Geología, Universidad Nacional del Sur, San Juan 670, B8000ICN Bahía Blanca, Argentina and [6]Institute for Earth Sciences, University of Graz, Heinrichstraße 26, 8010 Graz, Austria

*Corresponding author. Telephone: +43-1-4277-53318. E-mail: andrea.mundl@univie.ac.at

Received November 28, 2014; Accepted July 30, 2015

ABSTRACT

Alkali basalt hosted mantle xenoliths were sampled at four locations within the North Patagonian Massif, Argentina. The subcontinental lithospheric mantle (SCLM) beneath Comallo, Puesto Diaz and Cerro Chenque is mostly represented by spinel-harzburgites, whereas at Prahuaniyeu, spinel–garnet- and garnet-peridotites occur next to spinel-peridotites. Partial melting estimates for the north Patagonian mantle xenoliths determined from clinopyroxene trace element abundances reveal up to 25% melt extraction. Whereas the SCLM beneath Puesto Diaz, Cerro Chenque and Comallo is exclusively represented by highly depleted mantle xenoliths, the Prahuaniyeu sample suite comprises both fertile lherzolites and depleted harzburgites. Elevated trace element contents in all the studied north Patagonian mantle samples indicate that melt–rock interaction took place after an initial melt depletion event. Variable primitive mantle normalized REE patterns of clinopyroxenes from within one sample locality suggest compositional changes attributed to melt percolation, which has not significantly affected the bulk-rock and mineral major element compositions. Melt percolation processes have also been detected in the isotopic compositions of the xenoliths, as well as in their highly siderophile element systematics. Hf isotopic compositions are decoupled from those of Nd and Sr and have been affected by variable degrees of enrichment. Platinum group element (PGE) abundances also reveal indications of melt–rock reaction. In some samples this is reflected in fractionation of the iridium-group PGE and/or enrichment in the palladium-group PGE and/or rhenium, which cannot result merely from partial melting processes. Rhenium depletion ages (T_{RD}) determined from Os isotopic analyses reveal an at least late Paleoproterozoic (1·7 Ga) stabilization of the Prahuaniyeu SCLM. Mantle xenoliths sampled from beneath Comallo and Puesto Diaz–Cerro Chenque yield distinctly younger T_{RD} of 1·3 Ga and 1·0 Ga, respectively. Distinct differences in the character of mantle xenoliths from Prahuaniyeu and from Puesto Diaz and Cerro Chenque (i.e. SCLM stabilization age and range of fertility) suggest that at least two SCLM domains exist below the North Patagonian Massif.

Key words: metasomatism; Patagonia; radiogenic isotopes; Re–Os; SCLM

INTRODUCTION

Mantle xenoliths, fragments of the lithospheric mantle brought to the surface by volcanic eruptions, can provide detailed information on the evolution and geological history of lithospheric mantle domains. Several studies of alkali basalt hosted mantle xenoliths have been conducted over the past few decades to provide insights into the origin and geological history of the Patagonian lithosphere (e.g. Skewes & Stern, 1979; Stern *et al.*, 1989, 1999; Kempton *et al.*, 1999*a*, 1999*b*; Gorring & Kay, 2000; Rivalenti *et al.*, 2004; Bjerg *et al.*, 2005, 2009; Conceição *et al.*, 2005; Schilling *et al.*, 2005, 2008; Ntaflos *et al.*, 2007; Wang *et al.*, 2008; Mundl *et al.*, 2015). Bjerg *et al.* (2005) concluded that peridotites from northern Patagonia have generally experienced greater melt depletion than mantle xenoliths from southern Patagonia. Those researchers also demonstrated that intense cryptic and modal metasomatic events have affected the subcontinental lithospheric mantle (SCLM) in Patagonia. Rivalenti *et al.* (2004) noted an eastward fading slab imprint in the metasomatic agent affecting the SCLM of Patagonia. They also suggested differences in the extent of mantle wedge–melt interaction in northern and southern Patagonia, attributed to different properties of the subducting slab. On the basis of Re–Os isotopic data for Patagonian mantle xenoliths, Schilling *et al.* (2008) proposed Paleoproterozoic formation of the SCLM below Prahuaniyeu in the North Patagonian Massif (NPM) (Fig. 1) and proposed a connection to the Cuyania terrane, the Pampeia terrane or the Río de la Plata craton, all located to the north of the North Patagonian Massif. Those researchers also argued for the existence of younger Neoproterozoic lithospheric mantle below the rest of the North Patagonian Massif. From the Re–Os isotopic systematics of the mantle xenoliths Schilling *et al.* (2008) and Mundl *et al.* (2015) proposed a Mesoproterozoic stabilization age of the Deseado Massif SCLM, located to the south of the North Patagonian Massif. Mundl *et al.* (2015) suggested an even older (early to late Paleoproterozoic) stabilization of the SCLM to the south of the Deseado Massif.

The evolution of Patagonia is a matter of continuing discussion, with some interpretations favoring an allochthonous and others an autochthonous origin (Pankhurst *et al.*, 2006; Ramos, 2008; Rapalini *et al.*, 2010, 2013; and references therein). In this context, the accretionary history of the North Patagonian Massif and the Deseado Massif remain uncertain.

The combination of different radiogenic isotope systems (Os–Hf–Nd–Sr) provides an important tool with which to characterize the SCLM and potentially yields information on its age of stabilization and, hence, the timing of the formation of the SCLM beneath continental regions. In addition to lithophile major and trace element analyses, the study of highly siderophile elements (HSE) can be used to monitor melt-depletion events and provide better insights into metasomatic processes within the lithospheric mantle.

In this study we have conducted extensive geochemical and isotopic studies on mantle xenoliths collected at four locations within the North Patagonian Massif to contribute towards deciphering the character and the evolution of the SCLM in northern Patagonia.

GEOLOGICAL SETTING

Patagonia consists of three geographical provinces: Rio Negro in north Patagonia extends from 39° to 42°S, Chubut province from 42° to 46°S and the southernmost Santa Cruz province from 46° to 54°S. The evolution of the Andean Cordillera is related to the subduction of the Nazca plate in the north and the Antarctic plate in the south beneath the South American plate. The Cordillera is divided into the Southern Volcanic Zone (SVZ), which extends to 46°S, and the Austral Volcanic Zone (AVZ), from 49°S to 53°S (Stern *et al.*, 1999). These two zones are separated by a volcanic activity gap (VAG) that is probably due to the subduction of the Chile Ridge (Fig. 1; e.g. Ramos, 1999). The North Patagonian Massif (NPM) is located between 39° and 44°S (Fig. 1). Its northern border is represented by the Neuquén and Colorado basins. To the south, the North Patagonian Massif is separated from the Deseado Massif (Fig. 1) by the San Jorge basin. Martínez Dopico *et al.* (2011) suggested an age of basement formation of the North Patagonian Massif between 2·1 and 1·6 Ga, inferred from the Sm–Nd isotope characteristics of granites and orthogneisses. This Meso- to Paleoproterozoic basement is *inter alia* covered by voluminous products of various Phanerozoic magmatic events in northern Patagonia. The Meseta de Somuncura, a large volcanic province located between 40° and 43°S in the back-arc tectonic area east of the Andean Cordillera (Fig. 1), consists of late Oligocene–Miocene to Pliocene volcanic rocks (Kay *et al.*, 2007; Labudia *et al.*, 2011). The basement comprises late Precambrian to Paleozoic magmatic and metamorphic rocks that are covered by the extensive Jurassic silicic volcanic rocks of the Chon Aike province (e.g. Kay *et al.*, 1989; Pankhurst & Rapela, 1995) and Cretaceous to Tertiary volcanic and sedimentary rocks (e.g. Rapela & Kay, 1988; Rapela *et al.*, 1988; Ardolino *et al.*, 1999). Munoz *et al.* (2002) and Kay *et al.* (2007) suggested that a plume-like mantle upwelling was responsible for the extensive plateau lavas in this region. Postdating the Meseta volcanic rocks are late Pliocene to early Pleistocene alkali basaltic lava flows and cinder cones carrying mantle xenoliths.

ANALYTICAL METHODS

For bulk-rock analyses, the mantle xenolith samples were cut and any host basalt rims and surface alteration were completely removed. After drying, samples were

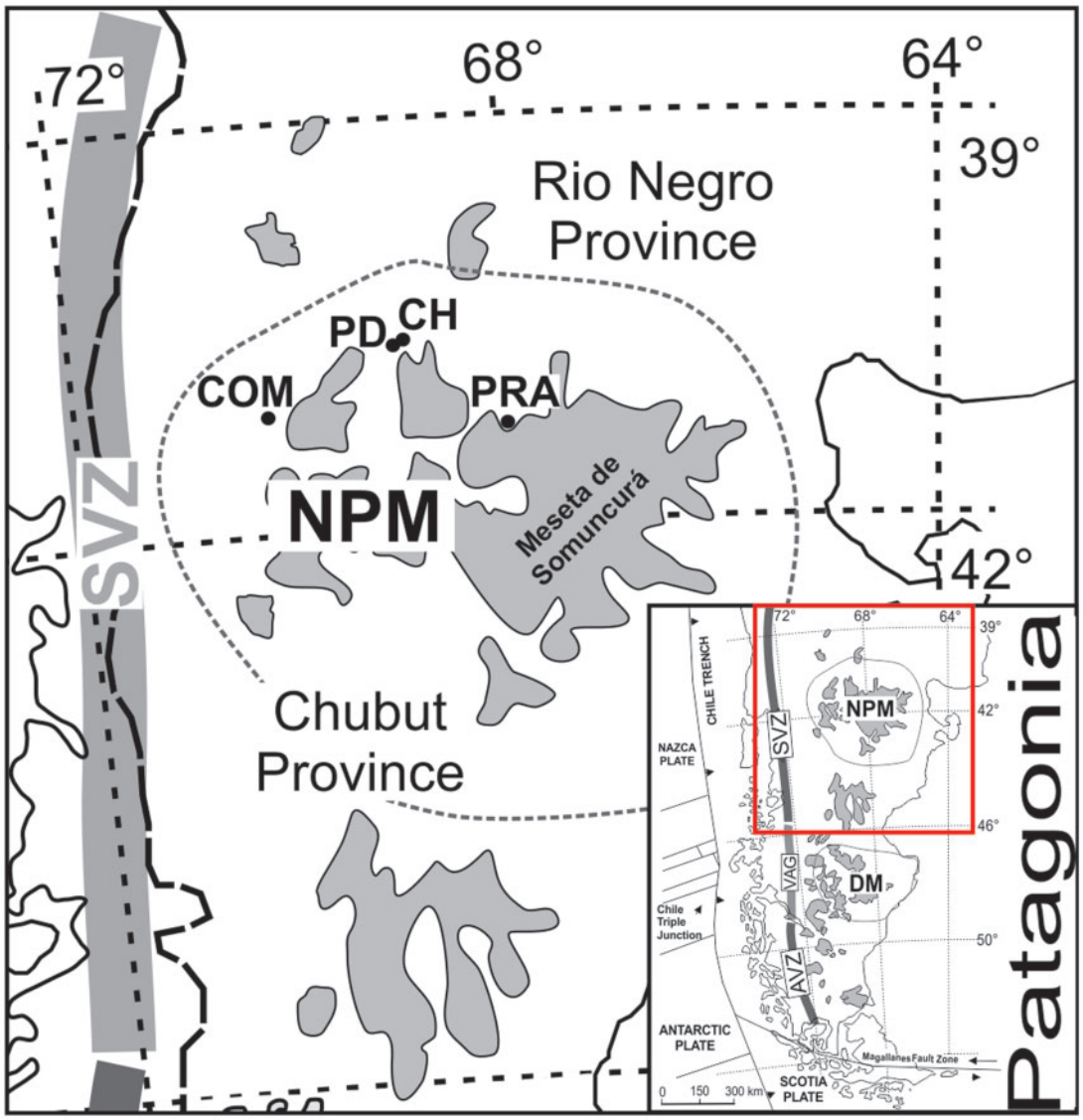

Fig. 1. Simplified map of north Patagonia, modified from Bjerg *et al.* (2009), showing the sample localities. Area within dark grey dashed line: North Patagonian Massif (NPM). Light grey fields represent Tertiary and Quaternary flood basalts. DM, Deseado Massif; AVZ, Austral Volcanic Zone; VAG, volcanic activity gap; SVZ, Southern Volcanic Zone. Mantle xenoliths were collected within the Rio Negro Province. Xenolith localities: CH, Cerro Chenque; PD, Puesto Diaz; COM, Comallo; PRA, Prahuaniyeu.

crushed and powdered in an agate mill. Bulk-rock major and trace elements were analyzed using a sequential Phillips PW 2400 X-ray spectrometer equipped with a Rh-excitation source at the University of Vienna, Department of Lithospheric Research. Fused disks for major element analyses were produced from a mixture of specimen and $Li_2B_4O_7$ flux, diluted 1:5. The trace elements Sc, Ni, Cr, Co, Zn and Ga were analyzed on pressed pellets. Replicate analyses of geo-standards GSR-3 gave an overall procedural uncertainty better than 2% for major elements and 5% (Cu = 8·5%) for trace elements. Bulk-rock powders were dissolved in an $HF–HNO_3$ 1:3 mixture and trace elements [rare earth elements (REE), high field strength elements (HFSE), large ion lithophile elements (LILE), U and Th] were analyzed in solution by inductively coupled plasma mass spectrometry (ICP-MS) (Agilent 7500) at the Central Laboratory for Water, Minerals and Rocks, NAWI Graz, Karl-Franzens-University of Graz and Graz University of Technology.

Mineral major element analyses were carried out using a Cameca SX100 electron microprobe at the Department of Lithospheric Research, University of Vienna. The operating conditions were 15 kV acceleration voltage and 20 nA beam current. Natural and synthetic standards were used for calibration and standard correction procedures were applied.

Bulk-rock osmium isotopic compositions and Re–Os concentrations were obtained at the Academy of Sciences of the Czech Republic (chemistry and ICP-MS) and at the Czech Geological Survey in Prague (negative thermal ionization mass spectrometry; N-TIMS).

The chemical procedures followed those of Ackerman *et al.* (2013). In brief, the samples were dissolved and equilibrated with a mixed ^{185}Re–^{190}Os and ^{191}Ir–^{99}Ru–^{105}Pd–^{194}Pt spikes using Carius tube technique (Shirey & Walker, 1995), followed by Os separation through solvent extraction by CCl_4 (Cohen & Waters, 1996) and Os microdistillation (Birck *et al.*, 1997). Iridium, ruthenium, platinum, palladium and rhenium were separated using anion exchange chromatography and then analyzed on a sector field ICP-MS Element 2 (Thermo) system coupled with an Aridus II^{TM} (CETAC) desolvating nebulizer. The Os isotopic compositions were determined by N-TIMS (Creaser *et al.*, 1991; Völkening *et al.*, 1991) using a Finnigan MAT 262 thermal ionization spectrometer. Rhenium depletion ages (T_{RD}; Walker *et al.*, 1989) were calculated using the primitive upper mantle values of Meisel *et al.* (2001): $^{187}Re/^{188}Os = 0{\cdot}4353$ and $^{187}Os/^{188}Os = 0{\cdot}1296$; $\lambda^{187}Re = 1{\cdot}666 \times 10^{-11}$ from Smoliar *et al.* (1996). Total procedural blanks were 0·1 pg for Os, 28 ± 32 pg for Ir, 28 ± 12 pg for Ru, 159 ± 82 pg for Pt, 110 ± 16 pg for Pd and 8 ± 6 pg for Re.

For Hf–Nd–Sr analyses, ~100 mg of optically pure clinopyroxene per sample were handpicked under a binocular microscope from the crushed peridotite samples at the University of Vienna, Department of Lithospheric Sciences. Spongy rims and inclusions were completely removed. The separates were then leached in hot 6N HCl overnight and dissolved in 4 ml of a mixture of concentrated HF–HNO_3 (1:3) for 3 days before being dried down.

The Hf isotope ratios were determined at the Center for Elemental Mass Spectrometry, University of South Carolina, using a NEPTUNE multicollector (MC)-ICP-MS system with the Plus option installed (Bizimis *et al.*, 2013; Mallick *et al.*, 2015). Hf was separated from the matrix on Ln resin (Eichrom, USA), following Munker *et al.* (2001). Sample introduction was through a 100 μl Teflon nebulizer coupled to an APEX system (ESI, USA). The measured ratios were corrected for mass fractionation using $^{179}Hf/^{177}Hf = 0{\cdot}7325$. The JMC-475 standard gave $^{176}Hf/^{177}Hf = 0{\cdot}282134 \pm 5$ ($n = 13$, ~35 ng Hf runs). All data are reported relative to the accepted JMC value of $^{176}Hf/^{177}Hf = 0{\cdot}282160$. Hf blanks were typically <50 pg.

Sr and Nd isotopic compositions were determined at the University of Vienna, Department of Lithospheric Research. About 50 mg of separated clinopyroxene was leached in hot 6 N HCl for 4 h before being dissolved in a HF–HNO_3 4:1 mixture, followed by dissolution in 1 ml of HNO_3 and subsequent transfer to 6N HCl. Element extraction (Sr, REE) was performed using AG 50 W-X8 (200–400 mesh, Bio-Rad) resin and 2·5N and 4·0N HCl as eluents. Nd was separated from the REE group using Teflon-coated HdEHP and 0·24N HCl as eluent. Maximum total procedural blanks were <1 ng for Sr and 50 pg for Nd, and were taken as negligible. The pure element fractions were evaporated using a Re double-filament assembly and run in static mode on a Thermo-Finnigan Triton TIMS system. A mean $^{87}Sr/^{86}Sr$ ratio of $0{\cdot}710280 \pm 0{\cdot}000006$ ($n = 7$) was determined for NBS987 (Sr) and a mean $^{143}Nd/^{144}Nd$ ratio of $0{\cdot}511850 \pm 0{\cdot}000003$ ($n = 7$) for La Jolla (Nd) international standards during the period of investigation. Within-run mass fractionation was corrected using $^{88}Sr/^{86}Sr = 8{\cdot}3752$ and $^{146}Nd/^{144}Nd = 0{\cdot}7219$, respectively.

Clinopyroxene trace elements were analyzed using a laser ablation (LA)-ICP-MS system (laser ablation unit: ESI NWR 193; ICP-MS system: Agilent 7500) at the Central Laboratory for Water, Minerals and Rocks, NAWI Graz, Karl-Franzens-University of Graz and Graz University of Technology. The material was ablated by using a 193 nm laser pulsed at 10 Hz with a 50–75 μm spot size and an energy of ~7 J cm^{-2}. Helium was used as the carrier gas at ~0·7 l min^{-1} flow rate and data were acquired in time-resolved mode. For each analysis a 30 s gas blank was obtained for background correction. A laser warmup for 30 s was done prior to ablation, which was active for 60 s followed by 60 s washout time. The standard glasses NIST610 or NIST612 were routinely analyzed for standardization using the values of Pearce *et al.* (1997) and drift correction, and standards NIST614 and BCR-2 were analyzed as unknowns to monitor the accuracy of the measurements. Both standards could be reproduced within ±10% of the certified values. Silicon or calcium was used as internal standard.

RESULTS

Sample description and petrography

Mantle xenolith samples for this study were collected from four localities in Rio Negro province, North Patagonian Massif (Fig. 1). Sample localities are Comallo (COM), located ~300 km east of the subduction zone front, Puesto Diaz (PD) and Cerro Chenque (CH), ~130 km NE of Comallo, and Prahuaniyeu (PRA), ~200 km E of Comallo. The COM samples were brought to the surface by lava flows, whereas mantle xenoliths from PD and CH were sampled from basaltic necks. In Prahuaniyeu, mantle xenoliths occur in nephelinites and tuffs. Host basalts from PD, CH and COM are of trachybasaltic composition. K/Ar dating of a Prahuaniyeu lava flow indicates an eruption age of $22{\cdot}2 \pm 0{\cdot}6$ Ma (unpublished data). The mantle xenolith carrying lava flow from Comallo has a K/Ar age of $1{\cdot}3 \pm 0{\cdot}4$ Ma (unpublished data). No age determinations for the host-rocks from Puesto Diaz and Cerro Chenque are available. However, K/Ar data for a basaltic neck at Traful, located 7–8 km SE of PD and CH, suggest an eruption age of $24{\cdot}2 \pm 0{\cdot}7$ Ma (unpublished data).

The studied sample suite comprises 28 spinel-harzburgites and two new spinel-dunites. Modal compositions (Table 1 and Fig. 2) were determined by mass balance of whole-rock and mineral compositions or by point counting (PD1, PD48 and PD61). Six additional spinel-harzburgites and one spinel–garnet-lherzolite (PRA74) were chosen from the large PRA sample suite

Table 1: Modal compositions of north Patagonian mantle xenoliths calculated using bulk-rock and mineral compositions

	Puesto Diaz								Cerro Chenque							
	PD1*	PD2	PD28	PD32	PD48*	PD51	PD61*	PD64	CH 1	CH17	CH25	CH26	CH42	CH43	CH48	CH63
Ol	75·5	75·6	75·5	78·4	87·3	76·3	73·4	77·5	76·4	64·0	78·5	65·0	81·5	81·1	92·7	73·8
Opx	20·3	21·6	21·6	19·1	3·5	21·0	22·1	19·4	21·2	33·6	19·9	32·2	16·5	16·8	1·2	23·3
Cpx	2·4	2·1	2·3	1·9	3·6	2·3	2·7	2·1	1·8	1·5	1·2	2·0	1·5	1·4	2·4	2·3
Spl	1·7	0·7	0·7	0·7	5·5	0·4	1·8	0·9	0·7	0·9	0·4	0·7	0·6	0·7	3·7	0·6
Grt	—	—	—	—	—	—	—	—	—	—	—	—	—	—	—	—
Rock type	H	H	H	H	D	H	H	H	H	H	H	H	H	H	D	H

	Comallo									Prahuaniyeu				
	COM101	COM103	COM108	COM110	COM118	COM139	COM140	COM141	COM142	*PRA74*	*PRA94*	*PRA301*	*PRA303*	*PRA306*
Ol	76·1	75·7	75·5	75·8	75·2	72·0	72·7	73·6	84·6	*64·6*	*77·8*	*69·8*	*70·8*	*72·1*
Opx	21·2	21·2	22·0	19·9	19·3	22·7	24·5	23·3	13·7	*23·3*	*19·5*	*26·1*	*24·6*	*24·3*
Cpx	1·9	2·1	1·7	3·3	4·6	4·6	1·9	2·5	1·0	*10·8*	*2·2*	*3·4*	*3·8*	*3·1*
Spl	0·9	1·0	0·8	0·9	0·9	0·7	0·9	0·6	0·8	*tr*	*0·5*	*0·5*	*0·5*	*0·5*
Grt	—	—	—	—	—	—	—	—	—	*1·6*	—	—	—	—
Rock type	H	H	H	H	H	H	H	H	H	L	H	H	H	H

*Modes determined by point counting method (1000 points per thin section).
H, harzburgite; D, dunite; L, lherzolite; Ol, olivine; Opx, orthopyroxene; Cpx, clinopyroxene; Spl, spinel; Grt, garnet; tr, traces. Samples in italic are data from Bjerg *et al.* (2009).

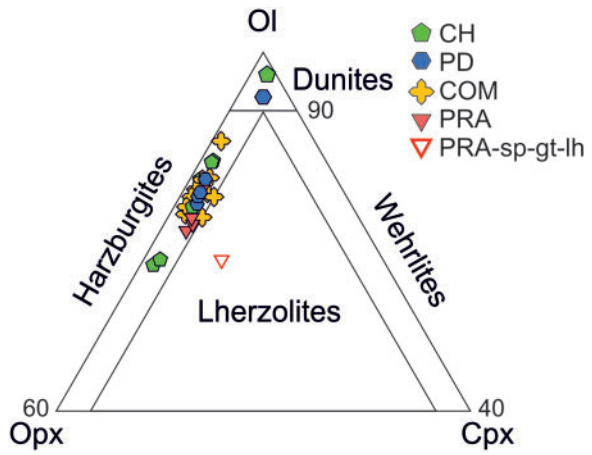

Fig. 2. Modal compositions of the north Patagonian mantle xenoliths calculated using mineral and bulk-rock major element compositions or determined by point counting. With the exception of samples PRA74 (spinel–garnet-lherzolite), PD48 and CH48 (spinel-dunites), all samples plot in the harzburgite field. Abbreviations as in Fig. 1.

previously studied by Bjerg *et al.* (2009) for further investigation. The COM and PRA samples are fresh, whereas samples from PD and CH have experienced minor serpentinization. Textures are mainly protogranular to porphyroclastic for PD and CH and protogranular to equigranular in COM and PRA; the latter often exhibit foliation defined by aligned elongated orthopyroxene and olivine (Fig. 3). Even though at the COM sample locality many peridotites contain disseminated amphibole and/or phlogopite, only anhydrous samples were chosen for this study. Hence, none of the samples exhibit obvious modal metasomatism. However, many samples contain thick melt veins (up to 100 μm) cutting through the host peridotite (Fig. 3e and f). These melt veins are dominantly filled with devitrified glass that sometimes contain tiny (~1 μm) Ni–Fe sulphides. In some samples, the veins are filled with silicate glass containing apatite, rutile and feldspar. Many samples show secondary textures, such as spongy rims around clinopyroxene, reaction rims around orthopyroxene and/or sieve-textured spinel. Deformation textures, such as kink bands in olivine or bent exsolution lamellae in orthopyroxene, are a common feature in north Patagonian mantle xenoliths.

Bulk-rock chemistry

Major and trace element data are given in Table 2. These include data for some PRA xenoliths previously reported by Bjerg *et al.* (2009).

Major elements

Bulk-rock Al_2O_3 and CaO contents of the studied samples lie within a narrow range of 0·68–1·31 wt % and 0·36–1·25 wt %, respectively. With the exception of sample PRA74, a spinel–garnet-lherzolite with Al_2O_3 and CaO contents of 2·78 wt % and 2·35 wt %, respectively, the studied samples represent an overall strongly depleted sample suite. Generally, there is a clear covariation between major elements. Al_2O_3 and CaO decrease with increasing MgO (Fig. 4a and b). The CaO contents of samples CH17, CH26 and CH48 are lower at a given MgO and deviate slightly from the apparent melt depletion trend defined by the remaining samples. Samples CH17 and CH26 have a high orthopyroxene/olivine ratio (~0·5), whereas sample CH48 probably represents a cumulate spinel-dunite. The deviation of these

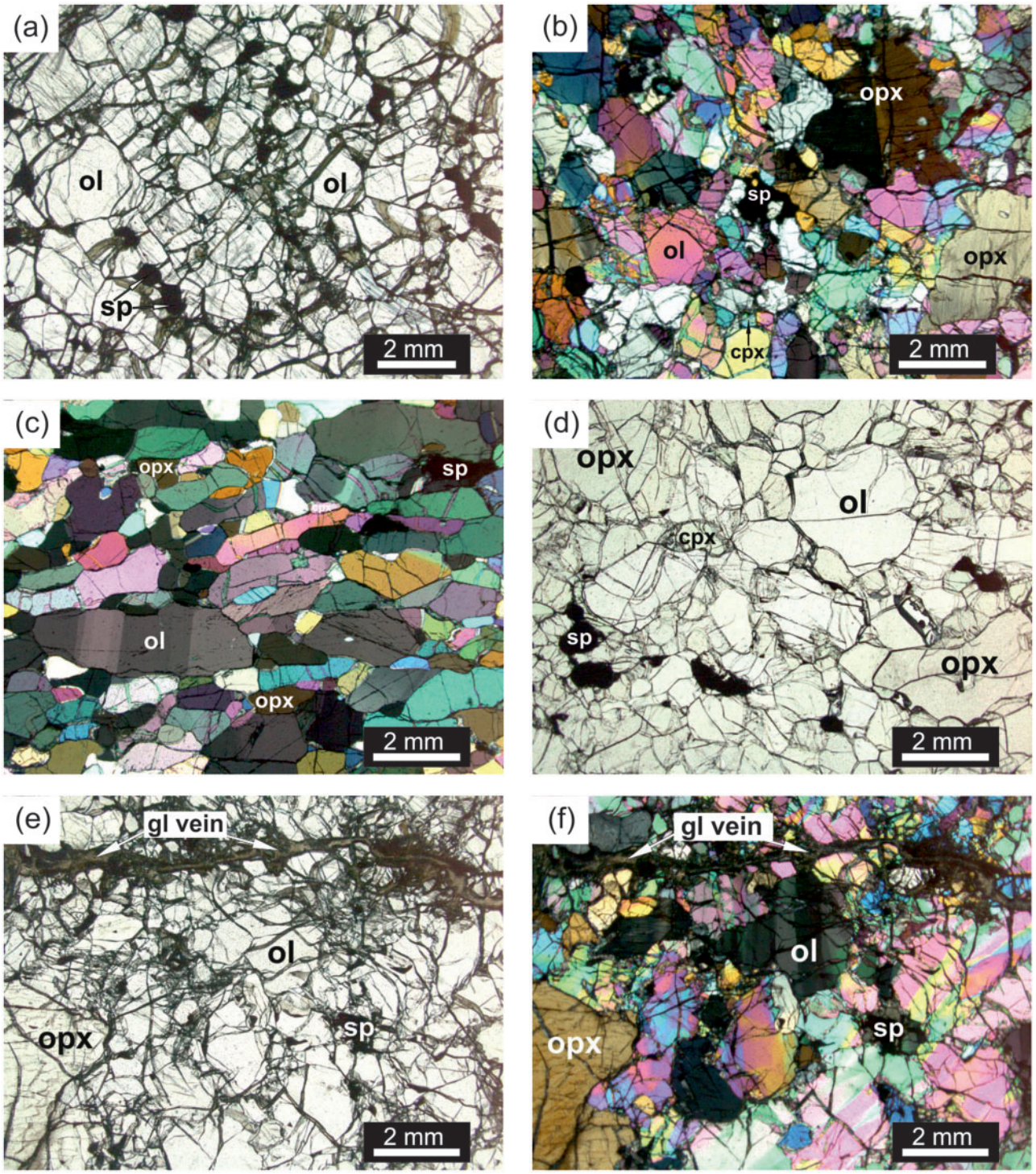

Fig. 3. Photomicrographs of north Patagonian mantle xenoliths. (a) Cumulate texture of dunite sample CH48 in plane-polarized light. (b) Protogranular texture of harzburgite CH25 under cross-polarized light; kink banded orthopyroxene and olivine should be noted. (c) Foliated texture of sample COM108 under cross-polarized light; ol exhibits kink bands. (d) Protogranular texture of sample COM141 in plane-polarized light. (e) Protogranular harzburgite PD64; thick devitrified glass vein should be noted. (f) Same as (e) under cross-polarized light. ol, olivine; opx, orthopyroxene; cpx, clinopyroxene; sp, spinel; gl vein, devitrified glass vein.

three samples from the rest of the sample suite is also illustrated in a plot of SiO_2 vs MgO (Fig. 4c). Whereas the cumulate dunite CH48 has a low bulk-rock SiO_2 content (40·0 wt %), samples CH17 and CH26 have higher SiO_2 for their MgO contents relative to the rest of the sample suite, reflecting the high orthopyroxene/olivine ratio. For comparison, fields for the Prahuaniyeu sample suite studied by Bjerg *et al.* (2009) and southern Patagonian mantle xenoliths from Mundl *et al.* (2015) are shown in Fig. 4a–c.

Table 2: Bulk-rock major and trace element compositions of PD, CH, COM and PRA samples

	Mantle xenoliths												
Rock type:	PD2[I] H	PD12[I] H	PD28[I] H	PD32[II] H	PD51[I] H	PD64[I] H	CH1[I] H	CH17[I] H	CH25[I] H	CH26[I] H	CH42[I] H	CH43[I] H	CH48[III] D
wt %													
SiO_2	44·9	44·5	44·8	44·2	44·6	44·3	44·8	46·7	44·9	46·8	44·0	45·7	40·0
TiO_2	0·005	0·001	0·002	0·013	0·023	0·003	0·003	0·003	0·006	0·007	0·007	0·002	0·057
Al_2O_3	0·88	0·74	0·94	0·74	1·04	0·83	0·87	1·26	0·84	1·03	0·68	0·91	1·31
FeO	7·11	7·28	7·10	7·59	7·90	7·63	7·19	6·50	7·59	6·92	7·37	6·82	14·16
MnO	0·11	0·11	0·12	0·12	0·12	0·12	0·11	0·11	0·12	0·12	0·11	0·11	0·17
MgO	46·3	46·2	46·1	46·4	46·0	46·3	46·7	45·0	46·8	44·8	47·2	45·8	44·7
CaO	0·66	0·84	0·65	0·62	0·64	0·63	0·53	0·56	0·45	0·67	0·51	0·58	0·61
Na_2O	<0·01	<0·01	<0·01	<0·01	<0·01	<0·01	<0·01	<0·01	<0·01	<0·01	<0·01	<0·01	<0·01
K_2O	0·006	0·020	0·007	0·023	0·017	0·012	0·007	0·005	0·008	0·010	0·012	0·005	0·004
P_2O_5	0·009	0·007	0·007	0·016	0·011	0·008	0·012	0·013	0·010	0·012	0·014	0·011	0·031
Total	100·01	99·74	99·70	99·72	100·41	99·82	100·29	100·08	100·65	100·34	99·84	99·89	100·99
Mg#	0·92	0·92	0·92	0·92	0·91	0·92	0·92	0·92	0·92	0·92	0·92	0·92	0·85
LOI%	0·69	0·53	0·70	0·60	1·01	0·45	0·46	0·39	0·60	0·56	0·27	0·69	0·82
ppm													
Sr	*0·582*	*1·920*	*1·859*	*2·926*	*1·824*	*<0·1*	*0·019*	*<0·1*	*<0·1*	*0·108*	*0·871*	*<0·1*	*3·935*
Ga	*2·3*	*2·3*	*2·8*	*2·9*	*2·6*	*2·2*	*2·0*	*2·9*	*2·8*	*4·1*	*9·0*	*2·6*	*4·4*
Zn	*63·5*	*75·7*	*66·2*	*68·6*	*74·2*	*69·9*	*65·3*	*61·3*	*60·2*	*63·6*	*66·7*	*66·6*	*139·7*
Ni	*2985*	*3055*	*2923*	*3026*	*2669*	*3035*	*3034*	*2702*	*2849*	*2690*	*3145*	*2820*	*2869*
Co	*184*	*188*	*183*	*199*	*195*	*197*	*187*	*165*	*190*	*168*	*198*	*172*	*336*
Cr	*3335*	*2986*	*3303*	*3212*	*2770*	*3916*	*3091*	*4036*	*3113*	*3982*	*3093*	*3564*	*6355*
Sc	*6·2*	*8·2*	*8·6*	*8·9*	*7·0*	*9·7*	*7·7*	*9·9*	*5·5*	*8·6*	*7·7*	*10·4*	*9·6*
V	*45·3*	*48·4*	*29·4*	*38·2*	*40·7*	*43·8*	*34·8*	*49·2*	*40·4*	*41·5*	*40·4*	*43·4*	*50·5*
Y	*<0·1*	*<0·1*	*<0·1*	*0·104*	*0·190*	*<0·1*	*0·010*	*<0·1*	*0·028*	*<0·1*	*<0·1*	*<0·1*	*0·228*
Nb	*0·006*	*<0·1*	*<0·1*	*0·562*	*0·126*	*0·008*	*0·066*	*0·001*	*0·027*	*0·050*	*0·138*	*<0·1*	*0·213*
La	*0·102*	*0·073*	*0·137*	*0·947*	*0·211*	*0·121*	*0·100*	*0·117*	*0·153*	*0·129*	*0·235*	*0·082*	*0·174*
Ce	*0·182*	*0·109*	*0·254*	*1·595*	*0·412*	*0·215*	*0·202*	*0·207*	*0·297*	*0·209*	*0·458*	*0·142*	*0·428*
Pr	*0·019*	*0·009*	*0·018*	*0·155*	*0·050*	*0·023*	*0·018*	*0·020*	*0·033*	*0·020*	*0·051*	*0·015*	*0·063*
Nd	*0·060*	*0·032*	*0·050*	*0·529*	*0·181*	*0·074*	*0·081*	*0·070*	*0·126*	*0·063*	*0·200*	*0·036*	*0·332*
Sm	*0·020*	*0·012*	*0·018*	*0·089*	*0·047*	*0·024*	*0·031*	*0·021*	*0·038*	*0·021*	*0·043*	*0·015*	*0·096*
Eu	*0·002*	*0·001*	*0·002*	*0·023*	*0·012*	*0·004*	*0·008*	*0·004*	*0·008*	*0·002*	*0·009*	*0·004*	*0·028*
Gd	*0·016*	*0·010*	*0·012*	*0·095*	*0·057*	*0·021*	*0·031*	*0·019*	*0·037*	*0·019*	*0·044*	*0·015*	*0·096*
Tb	*0·001*	*0·001*	*0·001*	*0·010*	*0·010*	*0·002*	*0·004*	*0·001*	*0·005*	*0·002*	*0·004*	*0·001*	*0·014*
Dy	*0·006*	*0·002*	*0·004*	*0·054*	*0·058*	*0·014*	*0·026*	*0·006*	*0·029*	*0·010*	*0·021*	*0·009*	*0·081*
Ho	*0·002*	*0·001*	*0·002*	*0·010*	*0·015*	*0·003*	*0·007*	*0·002*	*0·007*	*0·003*	*0·004*	*0·002*	*0·017*
Er	*0·006*	*0·001*	*0·006*	*0·033*	*0·040*	*0·010*	*0·017*	*0·006*	*0·024*	*0·009*	*0·011*	*0·006*	*0·046*
Tm	*0·001*	*0·001*	*0·002*	*0·004*	*0·007*	*0·003*	*0·003*	*0·002*	*0·005*	*0·002*	*0·003*	*0·001*	*0·007*
Yb	*0·015*	*0·010*	*0·020*	*0·034*	*0·063*	*0·020*	*0·028*	*0·016*	*0·036*	*0·019*	*0·021*	*0·013*	*0·055*
Lu	*0·003*	*0·002*	*0·003*	*0·005*	*0·010*	*0·003*	*0·005*	*0·002*	*0·007*	*0·002*	*0·003*	*0·002*	*0·009*
Hf	*0·04*	*0·03*	*0·05*	*0·06*	*0·08*	*0·05*	*0·04*	*0·03*	*0·04*	*0·04*	*0·05*	*0·03*	*0·10*
Ta	*<0·1*	*0·059*	*<0·1*	*<0·1*	*<0·1*	*<0·1*	*<0·1*	*<0·1*	*<0·1*	*0·069*	*0·003*	*<0·1*	*0·318*
Pb	*0·402*	*0·412*	*0·328*	*0·564*	*0·365*	*0·361*	*0·382*	*0·356*	*0·329*	*0·413*	*0·353*	*0·372*	*0·482*
Th	*0·028*	*0·034*	*0·067*	*0·152*	*0·046*	*0·038*	*0·214*	*0·032*	*0·041*	*0·055*	*0·046*	*0·040*	*0·036*
U	*0·047*	*0·077*	*0·031*	*0·042*	*0·034*	*0·037*	*0·059*	*0·017*	*0·019*	*0·029*	*0·034*	*0·026*	*0·026*

Trace elements

Primitive mantle (PM) normalized REE patterns can be used to divide the spinel-peridotite sample suite into three distinct groups (Fig. 5a–c). Group I is defined by a U-shaped REE pattern with strong enrichment in light REE (LREE) and minor enrichment in middle REE (MREE) relative to heavy REE (HREE) [$(La/Yb)_N = 2–14$; $(Sm/Yb)_N < 1–3$]. Group II samples exhibit a roughly linear enrichment from HREE to LREE [$(La/Sm)_N = 2–7$; $(Sm/Yb)_N = 1–3$] and samples from Group III display a hump in the MREE relative to the HREE and LREE [$(La/Sm)_N < 1$; $(Sm/Yb)_N = 2–3$]. The sole spinel–garnet-lherzolite sample PRA74 has a nearly flat PM-normalized REE pattern from HREE to MREE with a minor enrichment in La [$(La/Sm)_N = 1·3$] (Fig. 5d). All the studied samples exhibit elevated LREE and/or MREE. These enrichments contrast with the strong depletion signature recorded in the major element characteristics described above and therefore suggest that variable enrichment processes have occurred after the initial melt depletion event.

Mineral chemistry

Olivine

Olivine major element compositions are given in Table 3. Forsterite (Fo) contents in all samples fall in a narrow range between $Fo_{90·8–91·9}$ for spinel-harzburgites and $Fo_{90·5}$ for the spinel–garnet-lherzolite PRA74. Two cumulate dunites, PD48 and CH48, yield distinctly lower Fo contents of 86. The NiO and CaO compositions range from 0·37 to 0·45 wt % and 0·03 to 0·15 wt %, respectively in the mantle peridotites and from 0·30 to 0·32 wt % and 0·07 wt %, respectively, in the cumulate dunites.

Table 2: Continued

	Mantle xenoliths									
Rock type:	CH63[I] H	COM101[II] H	COM103[II] H	COM108[I] H	COM110[III] H	COM118[II] H	COM139[II] H	COM140[III] H	COM141[I] H	COM142[II] H
wt %										
SiO_2	45·1	44·2	44·8	44·2	44·2	44·7	45·5	45·3	45·3	43·8
TiO_2	0·008	0·030	0·020	0·027	0·043	0·070	0·036	0·027	0·003	0·018
Al_2O_3	0·71	0·95	0·98	0·91	1·04	1·30	1·14	1·25	0·87	0·68
FeO	7·65	7·86	7·48	7·71	7·73	7·17	7·44	7·47	7·13	7·14
MnO	0·12	0·12	0·12	0·12	0·12	0·12	0·12	0·12	0·12	0·11
MgO	45·6	45·8	45·9	45·9	45·4	45·7	45·3	45·7	45·7	48·0
CaO	0·69	0·60	0·65	0·56	0·94	1·19	1·25	0·63	0·74	0·36
Na_2O	<0·01	0·001	<0·01	0·001	0·001	<0·01	<0·01	<0·01	<0·01	<0·01
K_2O	0·007	0·005	0·015	0·010	0·009	0·060	0·014	0·003	0·003	0·012
P_2O_5	0·009	0·017	0·026	0·012	0·019	0·013	0·009	0·015	0·009	0·015
Total	99·85	100·21	100·80	100·04	100·09	101·15	101·63	101·28	100·80	101·03
Mg#	0·91	0·91	0·92	0·91	0·91	0·92	0·92	0·92	0·92	0·92
LOI%	1·07	–0·40	–0·41	–0·39	–0·42	–0·30	–0·22	–0·34	–0·33	–0·30
ppm										
Sr	*<0·1*	*4·488*	*5·409*	*4·112*	*7·140*	*15·018*	*7·933*	*2·581*	*7·777*	*2·970*
Ga	*3·4*	*1·0*	*2·7*	*0·6*	*1·3*	*2·8*	*2·8*	*3·4*	*2·1*	*2·5*
Zn	*65·0*	*46·9*	*69·4*	*46·2*	*47·8*	*65·7*	*67·9*	*69·9*	*65·0*	*66·6*
Ni	*3005*	*2362*	*2972*	*2371*	*2367*	*2933*	*2956*	*2844*	*2924*	*3173*
Co	*194*	*118*	*193*	*116*	*117*	*185*	*191*	*190*	*185*	*194*
Cr	*3094*	*2186*	*3417*	*2228*	*2322*	*2923*	*3148*	*3303*	*3487*	*3229*
Sc	*12·1*	*4·2*	*7·9*	*4·2*	*6·0*	*9·5*	*8·7*	*11·5*	*8·2*	*7·2*
V	*47·8*	*25·5*	*40·8*	*20·2*	*22·5*	*43·1*	*55·7*	*44·6*	*45·2*	*29·4*
Y	*<0·1*	*0·238*	*0·294*	*0·115*	*0·378*	*0·484*	*0·236*	*0·241*	*<0·1*	*0·127*
Nb	*0·174*	*0·037*	*0·119*	*0·094*	*<0·1*	*0·292*	*0·078*	*<0·1*	*<0·1*	*0·038*
La	*0·111*	*0·303*	*0·418*	*0·257*	*0·198*	*0·495*	*0·308*	*0·130*	*0·397*	*0·295*
Ce	*0·147*	*0·721*	*0·872*	*0·655*	*0·670*	*1·076*	*0·793*	*0·388*	*0·901*	*0·503*
Pr	*0·014*	*0·101*	*0·110*	*0·085*	*0·131*	*0·154*	*0·096*	*0·062*	*0·114*	*0·073*
Nd	*0·053*	*0·431*	*0·487*	*0·366*	*0·721*	*0·717*	*0·416*	*0·330*	*0·443*	*0·312*
Sm	*0·019*	*0·114*	*0·123*	*0·089*	*0·174*	*0·178*	*0·101*	*0·103*	*0·077*	*0·071*
Eu	*0·004*	*0·033*	*0·032*	*0·026*	*0·057*	*0·059*	*0·029*	*0·031*	*0·023*	*0·020*
Gd	*0·020*	*0·103*	*0·106*	*0·084*	*0·140*	*0·185*	*0·104*	*0·094*	*0·061*	*0·072*
Tb	*0·002*	*0·014*	*0·014*	*0·010*	*0·023*	*0·025*	*0·015*	*0·013*	*0·007*	*0·009*
Dy	*0·013*	*0·084*	*0·085*	*0·052*	*0·116*	*0·135*	*0·090*	*0·079*	*0·027*	*0·049*
Ho	*0·003*	*0·018*	*0·018*	*0·010*	*0·022*	*0·026*	*0·018*	*0·017*	*0·006*	*0·012*
Er	*0·008*	*0·051*	*0·050*	*0·030*	*0·059*	*0·073*	*0·050*	*0·050*	*0·017*	*0·035*
Tm	*0·003*	*0·009*	*0·008*	*0·006*	*0·009*	*0·012*	*0·007*	*0·009*	*0·003*	*0·006*
Yb	*0·019*	*0·059*	*0·055*	*0·036*	*0·056*	*0·070*	*0·052*	*0·060*	*0·026*	*0·035*
Lu	*0·004*	*0·010*	*0·009*	*0·006*	*0·010*	*0·010*	*0·008*	*0·010*	*0·004*	*0·006*
Hf	*0·05*	*0·17*	*0·15*	*0·09*	*0·12*	*0·10*	*0·08*	*0·09*	*0·09*	*0·08*
Ta	*0·004*	*0·028*	*<0·1*	*0·046*	*<0·1*	*0·066*	*<0·1*	*<0·1*	*<0·1*	*0·641*
Pb	*0·543*	*0·932*	*0·406*	*0·532*	*0·444*	*0·364*	*5·904*	*0·426*	*0·540*	*0·398*
Th	*0·042*	*0·054*	*0·070*	*0·052*	*0·034*	*0·047*	*0·039*	*0·035*	*0·044*	*0·052*
U	*0·062*	*0·031*	*0·044*	*0·023*	*0·022*	*0·027*	*0·027*	*0·016*	*0·022*	*0·026*

Orthopyroxene

Orthopyroxene compositions are given in Table 4. Orthopyroxenes in spinel-harzburgites with compositions $En_{89–91}Wo_{1–3}Fs_{8–9}$ have a narrow range of mg# [Mg/(Mg + Fe_{tot})] between 0·91 and 0·92. The spinel–garnet-lherzolite and the cumulate spinel-dunite have orthopyroxene compositions of $En_{89}Wo_2Fs_9$ with mg# 0·91 and $En_{85}Wo_1Fs_{14}$ with mg# 0·87, respectively. Orthopyroxene in spinel–garnet-lherzolite PRA74 has the highest Al_2O_3 content (5·7 wt %) of all analyzed orthopyroxenes.

Clinopyroxene

Major elements. Clinopyroxene major element compositions are given in Table 5. Clinopyroxene in the spinel-harzburgites is Cr-diopside with a mean composition of $En_{48–54}Wo_{42–49}Fs_{3–5}$ and mg# 0·91–0·95. Clinopyroxenes in the cumulate dunites are augite with a mean composition of $En_{46}Wo_{47}Fs_7$ and mg# 0·86. Cr_2O_3 contents vary between 0·71 and 1·24 wt % in the PD, CH and COM samples. Clinopyroxenes in the PRA samples have generally higher Cr_2O_3 contents from 1·11 to 1·53 wt % in spinel-peridotites. Na_2O and TiO_2 contents range from 0·27 to 1·48 wt % and from 0·01 to 0·86 wt %, respectively.

Trace elements. Based upon their trace element characteristics (Table 6), the clinopyroxenes can be divided into four groups (Fig. 6). Primitive mantle (PM) normalized trace element patterns of those samples also analyzed for their Sr–Nd–Hf isotopic compositions are highlighted. Group I is represented by samples with PM-normalized REE patterns showing a hump in MREE over HREE and LREE elements. Thus, $(La/Sm)_N < 1$ and

Table 2: Continued

	Mantle xenoliths					Host basalts			
Rock type:	PRA74^{III}* L	PRA94^{I}* H	PRA301^{I}* H	PRA303^{I}* H	PRA306^{II}* H	PD	CH	COM†	PRA*
wt %									
SiO_2	44·8	44·5	45·3	45·1	45·6	47·5	48·8	48·2	39·74
TiO_2	0·089	0·037	0·024	0·033	0·079	2·20	2·22	2·09	3·25
Al_2O_3	2·76	1·02	1·24	1·25	1·09	14·3	15·9	15·7	9·7
FeO	9·01	8·06	7·73	7·79	7·44	11·4	10·8	11·0	14·5
MnO	0·13	0·13	0·12	0·12	0·12	0·16	0·14	0·16	0·22
MgO	42·2	46·3	45·6	45·3	45·8	9·63	6·72	8·31	13·63
CaO	2·35	0·80	1·06	1·21	0·91	8·81	7·11	9·07	11·39
Na_2O	0·186	0·045	0·023	0·064	0·118	3·23	4·07	3·82	4·29
K_2O	0·013	0·068	0·005	0·027	0·019	2·17	2·73	1·49	1·20
P_2O_5	0·017	0·026	0·082	0·048	0·169	0·68	0·81	0·40	1·40
Total	100·77	100·99	101·15	100·91	101·28	100·07	99·26	100·17	99·26
Mg#	0·89	0·91	0·91	0·91	0·92	0·60	0·53	0·57	0·63
LOI%	*n.d.*	*n.d.*	*n.d.*	*n.d.*	*n.d.*	1·35	1·25	*n.d.*	0·47
ppm									
Sr	*n.d.*	*n.d.*	*n.d.*	*n.d.*	*n.d.*	911	930	550	1503
Ga	5·10	4·00	3·00	4·00	4·00	18	20	20	23
Zn	67	62	59	61	61	89	83	90	130
Ni	11·00	*n.d.*	*n.d.*	*n.d.*	n.d.	218	111	122	376
Co	2155	2353	2340	2372	2198	45	35	40	55
Cr	100	111	106	207	100	328	131	212	467
Sc	2952	2448	2820	2682	2780	8·1	5·7	23	17
V	8·30	6·00	6·20	6·30	7·10	195	141	190	170
Y	n.d.	n.d.	n.d.	n.d.	n.d.	20	23	24	43
Nb	n.d.	n.d.	n.d.	n.d.	n.d.	59	63	25	123
La	0·412	0·414	0·237	1·024	1·474	58	60	14	106
Ce	0·591	0·852	0·46	1·229	2·965	89	110	41	219
Pr	0·141	0·101	0·061	0·121	0·313	*n.d.*	*n.d.*	*n.d.*	*n.d.*
Nd	0·673	0·402	0·241	0·462	1·361	43	42	15	83
Sm	0·205	0·1	0·06	0·131	0·311	*n.d.*	*n.d.*	4·4	16
Eu	0·067	0·03	0·016	0·04	0·1	*n.d.*	*n.d.*	1·6	4·9
Gd	0·229	0·083	0·041	0·1	0·321	*n.d.*	*n.d.*	*n.d.*	*n.d.*
Tb	0·039	0·011	0·006	0·013	0·055	*n.d.*	*n.d.*	0·90	1·77
Dy	0·237	0·06	0·039	0·07	0·305	*n.d.*	*n.d.*	*n.d.*	*n.d.*
Ho	0·052	0·011	0·009	0·013	0·078	*n.d.*	*n.d.*	*n.d.*	*n.d.*
Er	0·14	0·048	0·03	0·042	0·231	*n.d.*	*n.d.*	*n.d.*	*n.d.*
Tm	0·022	0·009	0·006	0·009	0·039	*n.d.*	*n.d.*	*n.d.*	*n.d.*
Yb	0·13	0·067	0·048	0·05	0·264	*n.d.*	*n.d.*	1·9	2·56
Lu	0·02	0·011	0·01	0·01	0·04	*n.d.*	*n.d.*	0·19	0·28
Hf	*n.d.*	*n.d.*	*n.d.*	*n.d.*	*n.d.*	2·4	4·6	2·9	16·1
Ta	*n.d.*	*n.d.*	*n.d.*	*n.d.*	*n.d.*	3·2	4·3	*n.d.*	*n.d.*
Pb	*n.d.*	*n.d.*	*n.d.*	*n.d.*	*n.d.*	1·2	1·7	0·53	*n.d.*
Th	<0·01	0·11	0·06	0·15	0·02	7·4	9·0	3·0	*n.d.*
U	*n.d.*	*n.d.*	*n.d.*	*n.d.*	*n.d.*	*4·60*	*4·60*	*n.d.*	*n.d.*

PD, Puesto Diaz; CH, Cerro Chenque; COM, Comallo; PRA, Prahuaniyeu; rock types as in Table 1; italic values are ICP-MS analyses; others are XRF analyses; LOI, loss on ignition; n.d., not determined; superscript I, II and III are group affiliations according to PM-normalized REE patterns (Fig. 5).

*Bjerg *et al.* (2009).

†Ntaflos *et al.* (2000).

$(Sm/Yb)_N = 1·3–5·4$. All samples of this group exhibit negative Zr and Ti anomalies relative to the adjacent elements in their PM-normalized extended trace element patterns. Whereas some clinopyroxenes show either positive Pb (CH1) or positive Sr anomalies (COM108, COM118, COM142), the two cumulate dunites PD48 and CH48 exhibit both an enrichment in Sr as well as in Pb. The remaining clinopyroxenes from this group exhibit negative Sr and Pb anomalies. Samples from Group II display roughly flat REE patterns from HREE to MREE with $(Sm/Yb)_N \sim 1$ and an enrichment in LREE with $(La/Sm)_N = 1·3–4·1$. All samples from within this group exhibit negative Ti, Zr and Pb, and positive Sr anomalies. Group III samples are characterized by a continuous enrichment in MREE and LREE over HREE with $(Sm/Yb)_N = 2·7–5·9$ and $(La/Yb)_N = 6·6–18·1$, respectively. Normalized trace element patterns show positive as well as negative Pb and Sr and exclusively negative Zr anomalies in this clinopyroxene group. Clinopyroxenes from Group IV have U-shaped PM-normalized REE patterns that are defined by $(Ho/Yb)_N < 1$, an occasional minor enrichment in MREE with $(Sm/Yb)_N = 0·1–1·7$ and a strong enrichment in LREE with $(La/Yb)_N$ of up to 84·1. All Group IV clinopyroxenes show negative Zr anomalies and, with the exception of sample PRA301, clinopyroxenes from this group exhibit

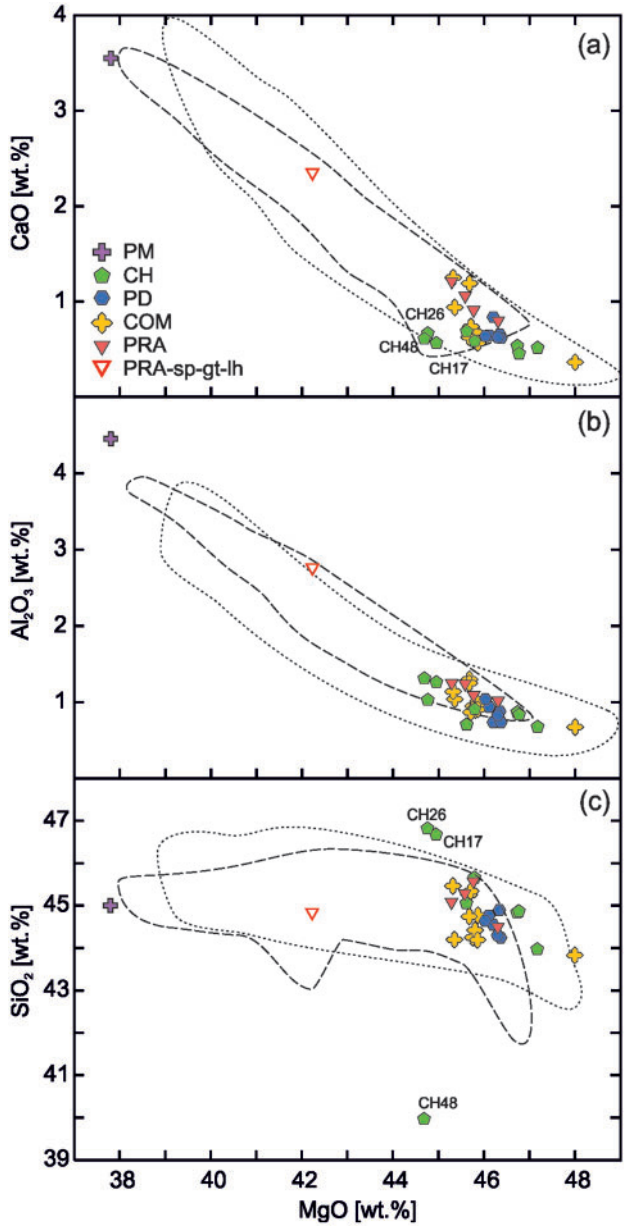

Fig. 4. Bulk-rock MgO vs CaO (a) Al_2O_3 (b) and SiO_2 (c) contents, respectively. Dashed line represents all Prahuaniyeu mantle xenoliths from Bjerg *et al.* (2009); dotted line represents bulk-rock compositions of southern Patagonian mantle xenoliths from Mundl *et al.* (2015). Samples CH48 (cumulate dunite), CH17 and CH26 deviate from the melting trends in (a) and (c). Legend and abbreviations as in Fig. 2; PM, primitive mantle from McDonough & Sun (1995).

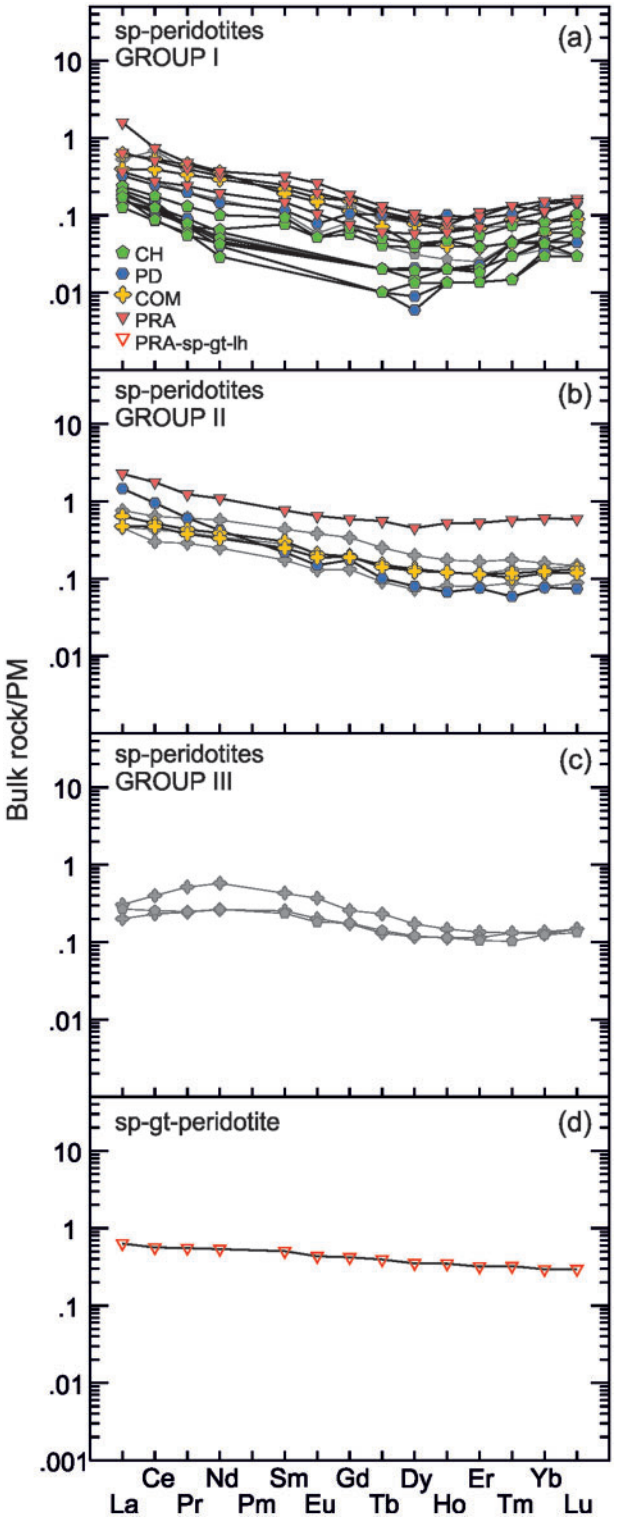

Fig. 5. Primitive mantle (PM) normalized bulk-rock rare earth element (REE) patterns. (a), (b) and (c) are for different groups of spinel-peridotite; (d) spinel–garnet-lherzolite. Plotted samples are those investigated for their Re–Os isotopic compositions and HSE contents in: (a) Group I: CH1, CH25, CH26, CH43, CH63, COM108, COM141, PD28, PD51, PD64, PRA94, PRA301, PRA303; (b) Group II: COM103, COM139, PD32, PRA306; (c) no Group III samples were analyzed for Re–Os or HSE; Group I, Group II and Group III are spinel-peridotites. Group IV comprises spinel–garnet-peridotite PRA74. Legend and abbreviations as in Fig. 2. PM from McDonough & Sun (1995).

negative Ti anomalies. Clinopyroxene from sample PRA74, the only spinel–garnet-peridotite within the sample suite, exhibits REE patterns expected for a fertile lherzolite and shows no enrichment in either MREE or LREE (Fig. 6e1 and e2).

Spinel

Representative spinel analyses are given in Table 7. Cr# [Cr/(Cr + Al)] and mg# in spinel are in the range of 0·23–

Table 3: Average olivine major element compositions determined using microprobe analysis

	PD1	PD2	PD7	PD27	PD28	PD32	PD48	PD51	PD61	PD64	CH1	CH12	CH17	CH25	CH26	CH42	CH43	CH48	CH63
n:	6	2	6	4	4	4	6	4	6	7	6	4	5	4	7	5	3	5	5
Rock type:	H	H	H	H	H	H	D	H	H	H	H	H	H	H	H	H	H	D	H
SiO_2	41·4	41·4	41·4	41·2	41·2	41·2	40·1	41·1	41·1	41·0	41·1	41·2	41·2	41·2	41·1	41·1	41·1	40·1	40·9
TiO_2	<0·01	<0·01	<0·01	0·01	0·01	<0·01	0·01	<0·01	0·01	0·01	<0·01	0·01	0·01	<0·01	0·01	0·01	0·02	0·01	0·01
Al_2O_3	<0·01	<0·01	<0·01	0·01	0·01	0·01	0·01	<0·01	<0·01	0·01	0·01	0·01	<0·01	<0·01	0·01	0·02	<0·01	0·01	0·01
Cr_2O_3	0·01	0·03	0·03	0·01	0·01	0·03	<0·01	<0·01	0·03	0·03	<0·01	0·01	0·01	<0·01	0·01	0·01	0·01	0·02	<0·01
FeO*	8·50	8·09	8·01	8·08	8·22	8·55	13·27	8·99	8·60	8·75	8·20	8·42	7·95	8·64	8·37	8·44	8·19	13·46	8·78
MnO	0·13	0·12	0·11	0·12	0·13	0·13	0·19	0·14	0·13	0·13	0·12	0·11	0·12	0·13	0·13	0·12	0·13	0·18	0·12
NiO	0·40	0·42	0·40	0·40	0·41	0·40	0·30	0·37	0·39	0·40	0·40	0·41	0·41	0·37	0·41	0·42	0·41	0·32	0·41
MgO	50·0	50·2	50·0	50·0	50·3	50·0	45·5	49·7	49·0	49·7	50·2	50·2	50·5	49·5	49·8	49·7	50·0	45·9	49·7
CaO	0·05	0·03	0·04	0·04	0·06	0·07	0·07	0·04	0·07	0·06	0·06	0·09	0·10	0·05	0·06	0·08	0·12	0·08	0·05
P_2O_5	<0·01	<0·01	<0·01	0·01	0·01	0·01	0·03	0·00	0·01	<0·01	<0·01	0·01	<0·01	0·01	0·01	<0·01	<0·01	0·04	0·01
Total	100·51	100·27	100·02	99·87	100·44	100·42	99·54	100·32	99·41	100·07	100·14	100·44	100·31	99·86	99·88	99·89	100·03	100·15	99·92
Mg#	0·91	0·92	0·92	0·92	0·92	0·91	0·86	0·91	0·91	0·91	0·92	0·91	0·92	0·91	0·91	0·91	0·92	0·86	0·91

	COM101	COM103	COM108	COM110	COM118	COM139	COM140	COM141	COM142	*PRA1*	*PRA74*	*PRA94*	*PRA301*	*PRA303*	*PRA306*
n:	>10	>10	>10	>10	>10	>10	>10	>10	>10						
Rock type:	H	H	H	H	H	H	H	H	H	*H*	*L*	*H*	*H*	*H*	*H*
SiO_2	41·0	41·2	41·0	41·0	41·1	40·9	41·0	41·2	41·3	*41·1*	*41·0*	*40·9*	*40·9*	*41·0*	*41·2*
TiO_2	0·01	<0·01	0·01	0·01	0·01	0·01	0·01	<0·01	0·01	*n.d.*	*n.d.*	*n.d.*	*n.d.*	*n.d.*	*n.d.*
Al_2O_3	0·04	0·01	0·03	0·02	0·03	0·01	0·01	0·01	0·01	*0·02*	*0·06*	*0·04*	*0·02*	*0·04*	*0·02*
Cr_2O_3	0·02	0·01	0·02	0·02	0·03	0·02	0·02	0·04	0·05	*0·05*	*0·01*	*0·05*	*0·05*	*0·04*	*0·03*
FeO*	8·52	8·52	8·41	8·53	8·39	8·56	8·59	8·30	7·84	*8·70*	*9·30*	*8·60*	*8·4*	*8·2*	*8·8*
MnO	0·13	0·13	0·13	0·13	0·13	0·13	0·12	0·12	0·12	*0·14*	*0·15*	*0·13*	*0·13*	*0·11*	*0·14*
NiO	0·41	0·40	0·42	0·42	0·39	0·39	0·39	0·40	0·40	*0·38*	*0·38*	*0·38*	*0·45*	*0·38*	*0·41*
MgO	49·9	49·6	50·2	49·7	49·8	49·6	49·6	49·7	50·0	*49·9*	*49·8*	*49·7*	*50·1*	*50·3*	*50·3*
CaO	0·06	0·06	0·06	0·07	0·07	0·07	0·07	0·07	0·08	*0·08*	*0·10*	*0·11*	*0·15*	*0·13*	*0·07*
P_2O_5	n.d.	0·023	*n.d.*	*n.d.*	0·01	0·01	0·01	0·01	0·01	*n.d.*	*n.d.*	*n.d.*	*n.d.*	*n.d.*	*n.d.*
Total	100·11	99·93	100·24	99·90	99·90	99·79	99·81	99·92	99·84	*100·35*	*100·69*	*99·98*	*100·24*	*100·21*	*100·97*
Mg#	0·91	0·91	0·91	0·91	0·91	0·91	0·91	0·91	0·92	*0·91*	*0·91*	*0·91*	*0·91*	*0·92*	*0·91*

*Total Fe as FeO.
n.d., not determined; samples in italic are from Bjerg *et al.* (2009); *n*, number of analyses; rock types as in Table 1.

0·49 and 0·64–0·78, respectively, in spinel-harzburgites. The cumulate dunites have spinels with cr# between 0·28 and 0·29; Mg# are in the range 0·51–0·54, much lower than for the harzburgites. Spinel in spinel–garnet-lherzolite PRA74 has the lowest cr# (0·19) and the highest mg# (0·81) of the entire sample suite.

Sulphides

Representative sulphide analyses are given in Table 8. Sulphide occurrences were investigated in 15 mantle peridotite samples, further used for Re–Os isotope analyses. All those samples contain sulphides, which occur either interstitially or enclosed, sometimes in the form of sulphide trails, primarily in olivine and orthopyroxene (Fig. 7a–f). In some samples, sulphides occur only as tiny (<2 μm) phases in intergranular devitrified glass; these are too small to be analyzed. Sulphides from eight samples were large enough to obtain good microprobe analyses (Table 8). The most abundant sulphide phases are monosulphide solid solution (Mss), pentlandite (Pn) and chalcopyrite (Cp). Other, less common, phases identified are pyrrhotite (Po, $Fe_{1-x}S_{(x=0-0.17)}$), bornite (Bn, Cu_5FeS_4), cubanite (Cb, $CuFe_2S_3$), pyrite (Py, FeS_2), heazlewoodite (Hz, Ni_3S_2) and millerite (Mi, NiS). In sample PD28, laurite, a rare ruthenium sulphide (RuS_2), was also found (Fig. 7c). No compositional differences between enclosed and interstitial sulphide phases of the same type can be recognized. Sulphides found in devitrified glass are commonly rich in Ni (up to 65 wt %) and were identified as heazlewoodite or millerite. Both enclosed and interstitial sulphides often exhibit rims or patches of secondary Fe-hydroxides, probably resulting from sulphur loss during weathering processes (Lorand, 1990).

P–T conditions

Equilibrium temperatures (Table 9), calculated using the two-pyroxene thermometer of Brey & Köhler (1990), at an assumed pressure of 15 kbar, yield core temperatures of up to ~950°C for samples from PD, CH and COM. Equilibration temperatures in PRA samples were determined by Bjerg *et al.* (2009) using the same method, yielding higher temperatures of up to ~1190°C relative to our studied mantle xenolith samples. Pressure estimated using the Al-in-opx geobarometer by Brey & Köhler (1990) for the only studied spinel–garnet-lherzolite is 22·4 kbar (Bjerg *et al.*, 2009).

Isotopic compositions and platinum group elements + Re systematics

Hf–Sr–Nd isotopic ratios

Hf, Sr and Nd isotopic data for leached clinopyroxene separates are given in Table 10 and plotted in Fig. 8. The 11 studied samples are exclusively spinel-harzburgites. For comparison, Sr–Nd isotopic data from Bjerg *et al.* (2009) for sample PRA74, a spinel–garnet-

Table 4: Average orthopyroxene major element compositions determined using microprobe analysis

	PD1	PD2	PD7	PD27	PD28	PD32	PD48	PD51	PD61	PD64	CH1	CH12	CH17
n:	4	4	3	6	4	6	3	4	8	6	4	5	5
Rock type:	H	H	H	H	H	H	D	H	H	H	H	H	H
SiO_2	57·2	56·9	57·2	57·2	56·9	56·8	55·4	55·8	56·7	57·1	56·7	56·7	56·9
TiO_2	0·10	0·01	0·01	0·01	0·01	0·01	0·19	0·14	0·02	0·01	0·03	0·01	0·01
Al_2O_3	2·49	2·33	2·10	2·11	2·24	2·11	2·61	3·44	2·16	1·83	2·22	2·27	2·21
Cr_2O_3	0·37	0·55	0·44	0·44	0·41	0·52	0·31	0·51	0·49	0·40	0·46	0·47	0·47
FeO*	5·46	5·41	5·24	5·29	5·22	5·53	8·81	5·96	5·45	5·53	5·30	5·47	5·21
MnO	0·13	0·13	0·13	0·14	0·13	0·16	0·19	0·15	0·13	0·13	0·13	0·14	0·13
NiO	0·09	0·08	0·09	0·08	0·11	0·10	0·06	0·06	0·11	0·09	0·09	0·09	0·09
MgO	34·7	35·0	34·6	34·8	34·7	34·6	32·0	34·0	34·2	34·9	34·6	34·6	35·0
CaO	0·34	0·37	0·52	0·33	0·58	0·63	0·44	0·41	0·62	0·42	0·51	0·57	0·43
Na_2O	0·04	0·02	0·01	0·02	0·09	0·01	0·04	0·01	0·07	0·02	0·02	0·02	0·02
Total	100·94	100·79	100·32	100·38	100·37	100·47	100·09	100·46	100·01	100·41	100·09	100·40	100·47
Mg#	0·92	0·92	0·92	0·92	0·92	0·92	0·87	0·91	0·92	0·92	0·921	0·919	0·92
en	91·1	91·2	91·1	91·4	91·0	90·5	85·6	90·1	90·5	90·9	91·1	90·4	91·4
wo	0·6	0·7	1·0	0·6	1·1	1·2	0·8	0·8	1·2	0·8	0·9	1·5	0·8
fs	8·2	8·1	7·9	8·0	7·9	8·3	13·5	9·1	8·3	8·3	8·0	8·2	7·8

	CH25	CH26	CH42	CH43	CH48	CH63	COM101	COM103	COM108	COM110	COM118	COM139
n:	7	4	5	5	3	6	>10	>10	>10	>10	>10	>10
Rock type:	H	H	H	H	D	H	H	H	H	H	H	H
SiO_2	56·4	57·1	57·0	56·9	55·3	57·3	56·6	56·7	56·5	56·4	56·4	56·0
TiO_2	0·07	0·02	0·01	0·01	0·21	0·01	0·03	0·04	0·03	0·07	0·08	0·06
Al_2O_3	2·87	1·96	1·85	2·19	2·61	1·45	2·40	2·17	2·34	2·56	2·65	2·63
Cr_2O_3	0·50	0·46	0·46	0·50	0·30	0·28	0·51	0·44	0·44	0·45	0·45	0·43
FeO*	5·75	5·53	5·31	5·22	8·92	5·64	5·48	5·51	5·52	5·39	5·34	5·65
MnO	0·14	0·14	0·13	0·12	0·19	0·13	0·14	0·13	0·14	0·14	0·13	0·13
NiO	0·08	0·10	0·09	0·09	0·08	0·11	0·10	0·10	0·11	0·11	0·1	0·1
MgO	34·1	34·7	34·9	34·8	32·0	35·1	34·4	34·2	34·5	34·2	34·3	34·1
CaO	0·48	0·36	0·57	0·56	0·60	0·39	0·64	0·62	0·63	0·66	0·64	0·63
Na_2O	0·03	0·02	0·02	0·02	0·04	0·03	0·02	0·05	0·13	0·01	0·06	0·04
Total	100·35	100·34	100·32	100·33	100·25	100·45	100·25	99·96	100·37	100·06	100·09	99·79
Mg#	0·91	0·92	0·92	0·92	0·86	0·92	0·92	0·92	0·92	0·92	0·92	0·92
en	90·3	91·0	91·0	91·1	85·2	90·9	90·5	90·5	90·5	90·5	90·7	90·2
wo	0·9	0·7	1·1	1·1	1·1	0·7	1·2	1·2	1·2	1·2	1·2	1·2
fs	8·8	8·4	8·0	7·8	13·6	8·4	8·3	8·4	8·3	8·2	8·1	8·6

	COM140	COM141	COM142	*PRA1*	*PRA74*	*PRA94*	*PRA301*	*PRA303*	*PRA306*
n:	>10	>10	>10						
Rock type:	H	H	H	*H*	*L*	*H*	*H*	*H*	*H*
SiO_2	56·0	56·8	57·0	*55·1*	*54·5*	*55·3*	*56·1*	*55·4*	*55·9*
TiO_2	0·06	0·01	0·05	*0·15*	*0·15*	*0·04*	*0·01*	*0·03*	*0·1*
Al_2O_3	2·83	2·05	1·97	*3·80*	*5·70*	*3·70*	*3·40*	*3·40*	*4·10*
Cr_2O_3	0·44	0·45	0·46	*0·81*	*0·65*	*0·92*	*0·66*	*1·04*	*0·59*
FeO*	5·63	5·40	5·02	*5·30*	*5·80*	*5·40*	*5·30*	*5·20*	*5·60*
MnO	0·12	0·13	0·12	*0·12*	*0·1*	*0·13*	*0·15*	*0·11*	*0·13*
NiO	0·10	0·10	0·10	*0·12*	*0·13*	*0·11*	*0·1*	*0·08*	*0·1*
MgO	33·9	34·4	34·5	*33·4*	*32·4*	*33·1*	*34·0*	*33·3*	*33·4*
CaO	0·62	0·58	0·62	*0·95*	*1·21*	*1·3*	*0·93*	*1·47*	*0·83*
Na_2O	0·06	0·04	0·08	*0·14*	*0·19*	*0·11*	*0·02*	*0·08*	*0·08*
Total	99·84	99·94	99·89	*99·87*	*100·73*	*100·12*	*100·67*	*100·08*	*100·84*
Mg#	0·92	0·92	0·92	*0·9*	*0·9*	*0·9*	*0·9*	*0·9*	*0·9*
en	90·2	90·7	91·2	*90·1*	*88·7*	*89·3*	*90·3*	*89·4*	*90·0*
wo	1·2	1·1	1·2	*1·8*	*2·4*	*2·5*	*1·8*	*2·8*	*1·6*
fs	8·6	8·2	7·6	*8·1*	*9·0*	*8·2*	*7·9*	*7·8*	*8·4*

*Total Fe as FeO.
Samples in italic are from Bjerg *et al.* (2009); *n*, number of analyses; rock types as in Table 1.

lherzolite, are also plotted. The Sr–Nd isotopic composition of the COM host basalt from Ntaflos *et al.* (2000) is also reported in Table 10 and plotted in Fig. 8.

The Sr and Nd isotopic compositions of the PD, CH and COM xenoliths are in the range of 0·703287–0·704835 and 0·512761–0·512952, respectively and plot between the Bulk Silicate Earth (BSE) and PREMA model compositions of Zindler & Hart (1986). The Prahuaniyeu samples have slightly lower $^{143}Nd/^{144}Nd$ (0·512620–0·513029) at a given $^{87}Sr/^{86}Sr$ (0·702663–0·703886) compared with the other studied samples. One sample, PRA301, has higher $^{143}Nd/^{144}Nd$ and lower $^{87}Sr/^{86}Sr$ than all the other samples and plots within the mid-ocean ridge basalt (MORB) field after Hofmann (1997).

The Hf isotopic results given in Table 10 show a wide range in radiogenic $^{176}Hf/^{177}Hf$ ratios. Samples from Comallo show narrow εHf values between +7·3

Table 5: Average clinopyroxene major element compositions determined using microprobe analysis

	PD1	PD2	PD7	PD27	PD28	PD32	PD48	PD51	PD61	PD64	CH1	CH12	CH17
n:	4	3	3	7	4	5	3	4	6	5	8	4	3
Rock type:	H	H	H	H	H	H	D	H	H	H	H	H	H
SiO_2	53·1	53·7	53·7	53·7	54·5	53·7	51·3	52·7	54·0	54·1	53·4	53·7	53·6
TiO_2	0·30	0·01	0·01	0·01	0·02	0·02	0·79	0·64	0·04	0·02	0·04	0·03	0·01
Al_2O_3	3·45	2·50	2·56	2·48	2·81	2·27	5·24	3·96	2·69	1·97	2·81	2·36	2·31
Cr_2O_3	0·91	1·01	0·99	0·96	1·05	0·96	0·99	0·81	1·07	0·71	1·12	0·85	0·81
FeO*	1·94	1·60	1·66	1·73	2·18	1·95	4·14	1·99	2·06	1·99	2·25	1·77	1·95
MnO	0·05	0·07	0·06	0·06	0·07	0·06	0·10	0·07	0·07	0·07	0·06	0·06	0·05
NiO	0·04	0·05	0·05	0·03	0·05	0·05	0·04	0·05	0·03	0·05	0·06	0·02	0·04
MgO	16·8	16·9	17·0	17·2	16·9	17·4	14·8	16·5	16·8	17·7	17·3	17·4	17·7
CaO	23·3	23·8	23·8	23·5	21·6	23·5	20·9	23·1	22·1	23·6	22·3	23·5	23·4
Na_2O	0·56	0·56	0·48	0·45	1·26	0·38	1·30	0·75	0·94	0·36	0·68	0·57	0·27
Total	100·54	100·18	100·21	100·16	100·47	100·26	99·56	100·50	99·86	100·60	100·00	100·17	100·14
Mg#	0·94	0·95	0·95	0·95	0·93	0·94	0·86	0·94	0·94	0·94	0·93	0·95	0·94
en	48·4	48·4	48·4	49·1	50·2	49·0	45·9	48·1	49·6	49·4	50·1	49·2	49·7
wo	48·4	49·0	48·8	48·1	46·1	47·8	46·7	48·5	46·9	47·4	46·1	47·9	47·1
fs	3·2	2·7	2·8	2·9	3·7	3·2	7·4	3·4	3·5	3·2	3·8	2·9	3·2

	CH25	CH26	CH42	CH43	CH48	CH63	COM101	COM103	COM107	COM108	COM110	COM118	COM139
n:	5	4	5	4	3	6	>10	>10	>10	>10	>10	>10	>10
Rock type:	H	H	H	H	D	H	H	H	H	H	H	H	H
SiO_2	53·0	53·6	53·7	53·9	51·2	53·7	53·3	53·5	54·4	53·2	53·1	52·7	52·5
TiO_2	0·25	0·04	0·01	0·01	0·86	0·05	0·10	0·10	0·08	0·09	0·20	0·28	0·22
Al_2O_3	4·03	2·32	2·15	2·28	5·04	2·26	3·02	2·95	3·24	3·22	3·33	4·17	3·31
Cr_2O_3	1·21	0·93	0·89	0·92	0·92	0·99	0·93	1·01	0·97	1·06	1·00	1·23	0·88
FeO*	1·85	1·80	2·08	1·89	4·19	1·85	2·38	2·41	2·31	2·55	2·41	2·40	2·59
MnO	0·08	0·06	0·07	0·07	0·09	0·06	0·08	0·07	0·08	0·07	0·08	0·07	0·07
NiO	0·03	0·05	0·04	0·06	0·03	0·05	0·05	0·05	0·07	0·05	0·04	0·06	0·06
MgO	15·9	17·1	17·8	17·4	14·7	17·1	16·9	16·7	16·3	16·7	16·8	16·2	16·7
CaO	22·8	23·5	22·9	23·0	21·5	23·6	22·5	22·0	21·1	22·1	22·5	21·7	22·5
Na_2O	0·94	0·50	0·40	0·51	1·28	0·56	0·74	0·96	1·48	1·11	0·75	1·11	0·71
Total	100·16	99·95	100·05	100·04	99·82	100·23	99·95	99·79	99·98	100·19	100·18	99·93	99·57
Mg#	0·94	0·94	0·94	0·94	0·86	0·94	0·93	0·93	0·93	0·92	0·93	0·92	0·92
en	47·6	48·8	50·2	49·6	45·2	48·7	49·1	49·2	49·7	49·1	48·9	48·9	48·6
wo	49·2	48·2	46·4	47·3	47·5	48·3	46·9	46·7	46·2	46·6	47·0	46·9	47·1
fs	3·3	3·0	3·4	3·1	7·4	3·1	4·0	4·1	4·1	4·3	4·1	4·2	4·4

	COM140	COM141	COM142	*PRA1*	*PRA74*	*PRA94*	*PRA301*	*PRA303*	*PRA306*
n:	>10	>10	>10						
Rock type:	H	H	H	*H*	*L*	*H*	*H*	*H*	*H*
SiO_2	52·6	53·5	53·9	*52·9*	*51·9*	*52·8*	*53·2*	*53·0*	*52·8*
TiO_2	0·23	0·01	0·14	*0·31*	*0·46*	*0·08*	*0·04*	*0·10*	*0·29*
Al_2O_3	4·11	2·96	3·24	*4·80*	*7·00*	*4·30*	*3·50*	*3·70*	*5·50*
Cr_2O_3	1·12	1·20	1·24	*1·50*	*1·08*	*1·53*	*1·11*	*1·51*	*1·22*
FeO*	2·57	2·30	2·24	*2·44*	*3·30*	*2·90*	*2·26*	*2·80*	*2·70*
MnO	0·07	0·07	0·07	*0·09*	*0·10*	*0·10*	*0·07*	*0·11*	*0·09*
NiO	0·05	0·05	0·05	*0·06*	*0·04*	*0·05*	*0·04*	*0·06*	*0·02*
MgO	16·1	16·6	16·3	*16·4*	*17·1*	*17·8*	*17·7*	*18·0*	*15·9*
CaO	21·7	22·1	21·1	*20·0*	*17·5*	*19·8*	*22·2*	*19·7*	*20·6*
Na_2O	1·11	0·97	1·46	*1·42*	*1·46*	*0·91*	*0·47*	*0·81*	*1·46*
Total	99·72	99·72	99·77	*99·96*	*99·89*	*100·24*	*100·50*	*99·77*	*100·59*
Mg#	0·92	0·93	0·93	*0·92*	*0·90*	*0·92*	*0·93*	*0·92*	*0·91*
en	48·6	49·0	49·8	*51·0*	*54·3*	*52·9*	*50·6*	*53·6*	*49·3*
wo	47·0	47·0	46·3	*44·7*	*39·9*	*42·2*	*45·7*	*42·0*	*46·1*
fs	4·5	3·9	4·0	*4·3*	*5·9*	*4·8*	*3·6*	*4·6*	*4·6*

*Total Fe as FeO.
Samples in italic are from Bjerg *et al.* (2009); *n*, number of analyses; rock types as in Table 1.

and +14·0 and yield unrealistic future T_{MA} values. The only Cerro Chenque sample analyzed for its Hf isotopic composition yields an εHf value of +37·8 and a T_{MA} of 0·38 Ga. The Puesto Diaz spinel-harzburgite PD32 has the highest $^{176}Hf/^{177}Hf$ of the whole sample suite at 0·28744, giving εHf of +164·8. The T_{MA} of sample PD32 is 1·1 Ga. The $^{176}Hf/^{177}Hf$ of sample PD51 gives εHf + 21·9 and a calculated T_{MA} of 1·2 Ga. The εHf values calculated from the Prahuaniyeu clinopyroxene separates are between +8·8 and +92·1 with T_{MA} values ranging from unrealistic future to impossibly old ages. Overall, Hf isotopes show a strong decoupling from

Table 6: Cpx and gt trace element compositions determined using ICP-MS laser ablation analysis

	sp-peridotites																	
	PD1^{I}	PD7^{IV}	PD27^{IV}	PD28^{IV}	PD32^{IV}	PD48^{I}	PD 51^{I}	PD61^{II}	PD64^{IV}	CH1^{I}	CH12^{IV}	CH17^{IV}	CH25^{II}	CH26^{IV}	CH42^{IV}	CH43^{IV}	CH48^{I}	CH63^{II}
Co	20·3	19·7	21·0	20·4	19·6	21·5	20·5	18·5	17·5	19·7	20·4	20·9	19·2	17·0	19·9	20·9	18·0	31·4
Zn	18·40	10·27	16·45	8·24	8·30	13·83	14·54	8·61	8·62	7·27	8·87	7·57	6·02	15·86	7·39	8·09	14·86	11·96
Cu	2·478	3·655	1·905	3·170	3·970	1·580	0·606	1·168	0·959	1·498	0·919	1·157	0·972	0·969	1·500	1·748	1·037	1·421
V	271	143	156	133	167	245	224	183	180	175	188	146	204	124	196	158	229	197
Rb	<0·025	0·147	0·085	0·057	0·063	0·074	<0·028	0·056	0·059	0·056	0·079	0·035	<0·030	<0·023	<0·026	0·077	0·030	0·225
Sr	34·5	4·5	7·0	4·0	5·8	333·0	50·2	37·5	10·1	33·8	14·5	0·9	38·4	6·8	26·9	3·4	265·2	10·9
Y	6·22	1·01	0·66	0·80	0·87	15·68	11·91	4·15	1·62	5·81	1·18	0·22	5·94	1·58	0·95	0·54	16·36	1·58
Zr	12·21	0·03	0·13	3·15	0·02	49·05	14·20	3·05	0·84	9·19	0·96	0·02	3·38	1·84	0·50	0·10	49·88	1·56
Ba	0·027	0·046	1·046	<0·068	<0·074	0·198	<0·068	0·030	<0·023	0·084	0·158	0·146	<0·084	0·098	<0·076	0·841	0·020	0·461
Nb	0·197	0·034	0·098	0·114	0·050	0·069	0·152	0·624	0·135	0·135	0·467	0·012	0·205	0·027	0·237	0·018	0·056	0·237
La	1·031	0·115	0·242	3·710	4·900	2·838	0·826	3·395	0·761	0·450	0·818	0·120	1·789	0·597	1·907	0·121	2·390	0·462
Ce	3·650	0·387	0·659	5·760	7·560	11·818	3·165	7·480	1·770	1·836	1·890	0·129	5·045	0·778	4·440	0·152	10·105	0·877
Pr	0·619	0·054	0·084	0·364	0·560	2·107	0·649	0·724	0·200	0·395	0·228	<0·007	0·740	0·077	0·551	0·015	2·040	0·124
Nd	3·483	0·281	0·354	0·708	1·241	11·880	4·150	2·515	0·633	2·337	1·172	<0·033	3·455	0·330	1·758	0·093	11·425	0·727
Sm	1·178	0·071	0·084	0·120	0·098	3·440	1·566	0·526	0·111	0·846	0·290	<0·048	0·866	0·127	0·312	0·059	3·260	0·210
Eu	0·456	0·026	0·032	0·017	0·043	1·181	0·561	0·212	0·056	0·307	0·089	<0·013	0·305	0·053	0·090	<0·013	1·080	0·071
Gd	1·374	0·076	0·074	0·054	0·073	3·445	2·174	0·531	0·164	1·008	0·248	<0·049	0·900	0·192	0·182	0·052	3·455	0·228
Tb	0·217	0·019	0·011	0·012	0·012	0·511	0·383	0·096	0·028	0·173	0·034	<0·006	0·159	0·027	0·020	0·007	0·467	0·045
Dy	1·353	0·141	0·098	0·052	0·110	3·248	2·630	0·622	0·182	1·079	0·212	<0·023	1·022	0·256	0·154	0·071	3·100	0·262
Ho	0·258	0·037	0·024	0·017	0·027	0·632	0·496	0·139	0·057	0·224	0·041	0·008	0·219	0·055	0·027	0·015	0·659	0·061
Er	0·624	0·123	0·088	0·101	0·109	1·691	1·297	0·441	0·174	0·613	0·136	0·052	0·634	0·175	0·112	0·091	1·741	0·175
Tm	0·073	0·022	0·017	0·021	0·021	0·232	0·177	0·066	0·024	0·079	0·024	0·010	0·095	0·025	0·024	0·017	0·241	0·020
Yb	0·493	0·216	0·157	0·239	0·193	1·603	1·064	0·476	0·232	0·547	0·188	0·115	0·627	0·209	0·199	0·133	1·780	0·214
Lu	0·069	0·034	0·029	0·049	0·035	0·234	0·143	0·065	0·044	0·081	0·032	0·020	0·111	0·032	0·033	0·024	0·250	0·034
Hf	0·318	<0·009	0·006	<0·025	0·023	1·681	0·340	0·047	0·012	0·063	0·007	0·020	0·035	0·084	<0·024	0·022	1·652	0·101
Ta	0·056	0·006	0·023	0·021	<0·006	0·011	0·024	0·030	0·019	0·013	0·031	<0·008	0·024	0·002	0·049	<0·006	0·013	0·026
Pb	0·072	0·176	0·046	1·293	0·439	2·760	0·068	0·371	0·035	0·821	0·061	0·147	0·096	0·613	0·162	0·314	3·160	0·165
Th	0·034	0·003	0·013	1·689	0·594	0·045	0·017	0·741	0·006	0·164	0·144	<0·009	0·039	0·127	0·057	0·023	0·104	0·056
U	0·013	<0·002	0·007	0·859	0·113	0·042	0·011	0·228	0·006	0·027	0·052	<0·001	0·020	0·210	0·026	0·061	0·046	0·013

Table 6: Continued

	sp-peridotites											sp–gt-lherzolite	
	COM103[I]	COM108[I]	COM118[I]	COM139[III]	COM140[I]	COM141[III]	COM142[I]	*PRA1*[I]	PRA94[III]	*PRA301*[IV]	PRA303[IV]	*PRA74 cpx*	*PRA74 gt*
Co	19·9	20·8	19·5	21·0	19·8	18·6	18·9	*22·1*	n.d.	*18·8*	n.d.	*25·8*	*43·5*
Zn	8·72	9·72	8·92	9·51	9·13	7·21	7·80	*n.d.*	n.d.	*n.d.*	n.d.	*n.d.*	*n.d.*
Cu	0·754	0·609	1·018	0·661	1·701	0·257	2·246	*n.d.*	n.d.	*n.d.*	n.d.	*n.d.*	*n.d.*
V	191	203	223	229	250	234	190	*193*	n.d.	*163*	n.d.	*193*	*98*
Rb	0·022	<0·035	0·025	<0·029	0·033	<0·023	<0·025	*0·010*	0·043	*0·027*	0·007	*0·010*	*0·020*
Sr	141·5	192·4	253·3	203·6	202·6	211·6	225·3	*112·3*	144·6	*45·1*	31·3	*74·9*	*0·313*
Y	9·86	5·95	10·64	6·84	11·95	2·23	10·17	*4·47*	4·88	*1·46*	0·86	*6·26*	*42·87*
Zr	67·19	58·28	37·42	39·17	48·34	35·16	30·13	*18·23*	8·39	*0·16*	0·13	*16·03*	*34·83*
Ba	<0·053	0·018	<0·075	<0·066	0·071	<0·062	0·066	*0·115*	1·009	*0·063*	0·050	*0·213*	*0·023*
Nb	0·064	0·132	0·229	0·120	0·075	0·202	0·113	*0·340*	1·191	*0·165*	2·118	*0·278*	*0·153*
La	2·052	2·804	4·060	5·183	3·223	6·530	1·886	*1·367*	4·880	*0·737*	1·840	*1·075*	*0·010*
Ce	9·497	9·900	14·530	13·190	13·147	17·630	10·075	*5·457*	10·773	*1·720*	2·075	*3·835*	*0·127*
Pr	1·966	1·643	2·553	1·851	2·583	2·306	2·056	*1·027*	1·265	*0·188*	0·103	*0·703*	*0·053*
Nd	11·640	8·094	12·647	8·290	14·700	9·327	11·730	*5·233*	5·663	*0·543*	0·200	*3·810*	*0·550*
Sm	3·417	1·969	3·027	1·825	4·100	1·367	3·030	*1·473*	1·223	*0·045*	0·014	*1·300*	*0·707*
Eu	1·052	0·628	1·004	0·625	1·305	0·526	1·028	*0·550*	0·404	*0·010*	0·008	*0·525*	*0·473*
Gd	3·037	1·661	2·760	1·841	3·653	0·907	3·095	*1·090*	1·056	*0·040*	0·016	*1·443*	*2·520*
Tb	0·428	0·233	0·414	0·270	0·486	0·097	0·403	*0·147*	0·152	*0·010*	0·005	*0·255*	*0·570*
Dy	2·186	1·314	2·321	1·573	2·718	0·472	2·292	*0·877*	0·941	*0·147*	0·080	*1·715*	*5·483*
Ho	0·391	0·235	0·431	0·292	0·494	0·083	0·414	*0·183*	0·187	*0·045*	0·029	*0·290*	*1·563*
Er	0·978	0·603	1·114	0·748	1·323	0·233	0·993	*0·487*	0·527	*0·175*	0·136	*0·725*	*5·427*
Tm	0·121	0·075	0·145	0·089	0·165	0·033	0·120	*0·097*	0·073	*0·032*	0·027	*0·080*	*0·930*
Yb	0·701	0·490	0·877	0·567	1·040	0·259	0·779	*0·547*	0·493	*0·283*	0·238	*0·310*	*7·487*
Lu	0·095	0·067	0·115	0·076	0·138	0·042	0·099	*0·083*	0·072	*0·050*	0·042	*0·035*	*1·110*
Hf	2·383	1·583	1·282	0·692	1·590	0·584	1·132	*0·483*	0·273	*0·010*	0·004	*0·508*	*0·553*
Ta	0·034	0·041	0·044	0·062	0·034	0·212	0·030	*0·030*	0·110	*0·010*	0·081	*0·023*	*0·010*
Pb	0·145	0·165	0·220	0·243	0·100	0·400	0·067	*n.d.*	0·030	*n.d.*	0·044	*<0·010*	*<0·010*
Th	0·154	0·232	0·192	0·243	0·278	0·389	0·053	*0·027*	0·338	*0·037*	0·205	*0·023*	*0·010*
U	0·080	0·091	0·089	0·086	0·079	0·150	0·033	0·040	0·082	0·010	0·068	0·010	n.d.

Samples in italic are from Bjerg *et al.* (2009); superscript I, II, III and IV are group affiliations according to PM-normalized REE patterns (Fig. 6).

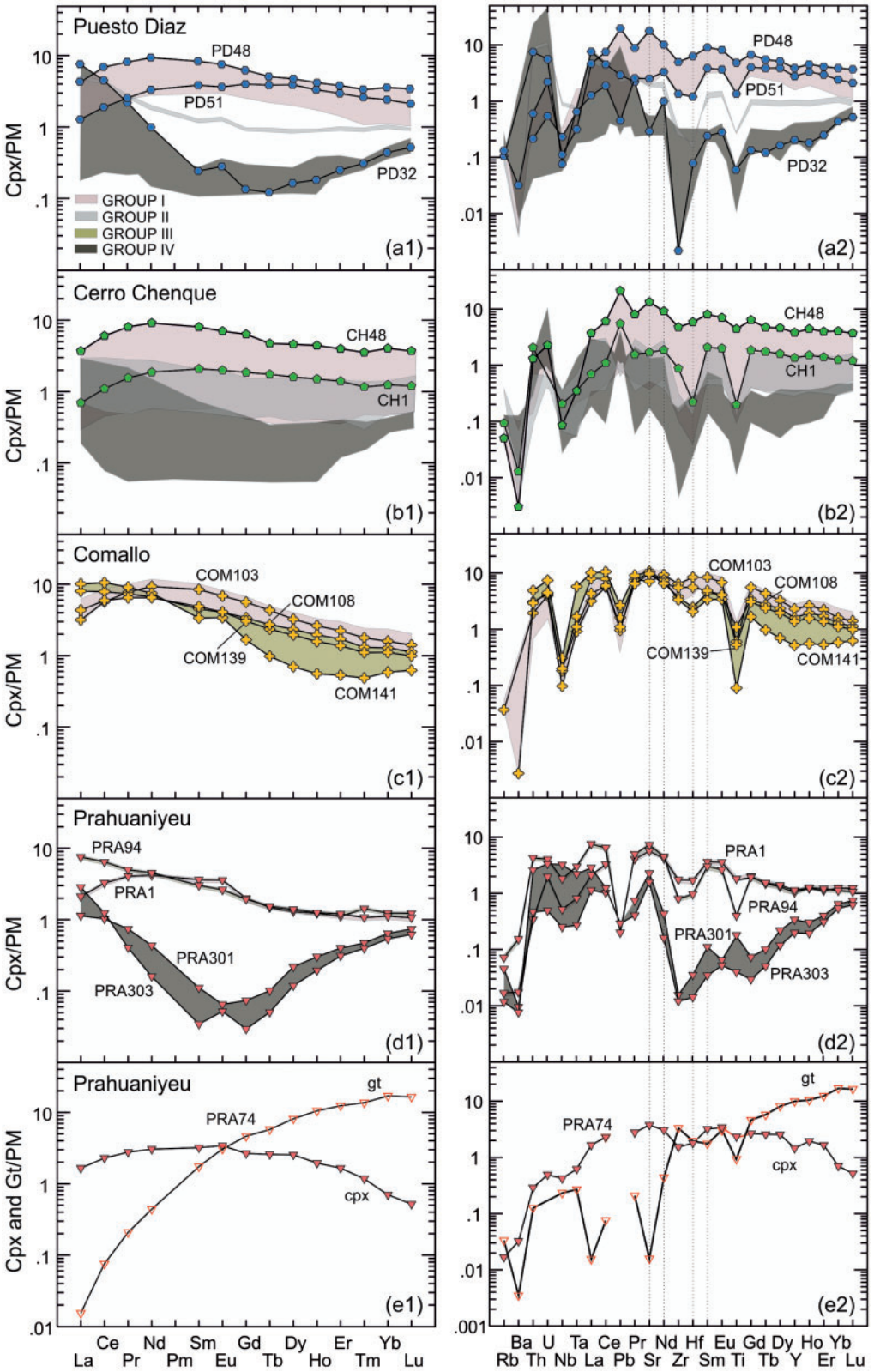

Fig. 6. Primitive Mantle (PM) normalized clinopyroxene and garnet REE and trace element patterns subdivided by sampling locality: Puesto Diaz (a1 and a2), Cerro Chenque (b1 and b2), Comallo (c1 and c2) and Prahuaniyeu (d1 and d2). Different shaded fields represent the four separate groups. Each group contains samples with distinct PM-normalized REE and trace element patterns. Group I: LREE < MREE > HREE; Group II: LREE > MREE = HREE; Group III: LREE > MREE > HREE; Group IV: LREE ≫ MREE \II HREE. Samples analyzed for their isotopic composition are highlighted. (e1) and (e2) are PM-normalized REE and trace element patterns for cpx and gt from spinel–garnet-lherzolite PRA74. Symbols and abbreviations as in Fig. 2.

Table 7: Average spinel major element compositions determined using microprobe analysis

	PD1	PD2	PD7	PD27	PD28	PD32	PD48	PD51	PD61	PD64	CH1	CH12	CH17	CH25	CH26	CH42	CH43	CH48	CH63
n:	2	3	2	2	2	2	3	4	4	3	5	5	4	3	3	3	2	5	4
Rock type:	H	H	H	H	H	H	D	H	H	H	H	H	H	H	H	H	H	D	H
SiO_2	0·07	0·02	0·07	0·06	0·02	0·07	0·09	0·03	0·04	0·03	0·04	0·04	0·03	0·01	0·03	0·06	0·05	0·05	0·03
TiO_2	0·58	0·02	0·01	<0·01	0·01	0·04	0·74	0·16	0·21	0·02	0·04	0·14	0·04	0·14	0·04	0·70	0·01	2·09	0·07
Cr_2O_3	28·4	34·4	34·6	36·4	32·6	34·7	21·3	21·0	38·0	35·9	32·5	34·5	32·3	27·5	38·3	38·1	37·7	21·4	37·8
Al_2O_3	39·6	35·7	34·5	33·8	37·2	33·9	37·6	47·5	29·6	33·5	36·5	34·4	37·1	41·0	30·6	28·1	31·2	35·0	31·2
FeO	10·3	11·3	11·6	10·8	10·5	10·8	15·1	9·8	11·2	11·6	10·2	10·6	10·0	9·9	11·1	12·1	11·2	16·9	12·1
Fe_2O_3	1·43	0·62	1·10	0·47	0·90	2·43	8·77	1·22	2·95	1·37	2·28	1·90	1·19	1·67	2·15	3·77	2·25	8·76	1·69
MgO	18·2	17·0	16·6	17·0	17·6	17·1	15·0	19·2	16·4	16·5	17·8	17·3	17·9	18·5	16·6	16·0	16·6	14·3	16·0
MnO	0·13	0·11	0·11	0·10	0·10	0·14	0·14	0·10	0·13	0·14	0·11	0·12	0·10	0·13	0·12	0·13	0·12	0·16	0·13
NiO	0·21	0·16	0·17	0·16	0·20	0·18	0·29	0·22	0·17	0·18	0·20	0·21	0·20	0·14	0·15	0·20	0·17	0·30	0·17
Total	98·97	99·42	98·72	98·79	99·16	99·36	99·05	99·21	98·67	99·25	99·63	99·24	98·89	98·89	99·10	99·29	99·18	98·91	99·05
Mg#	0·74	0·72	0·70	0·73	0·73	0·71	0·54	0·76	0·68	0·70	0·72	0·72	0·74	0·74	0·69	0·65	0·69	0·51	0·68
Cr#	0·32	0·39	0·40	0·42	0·37	0·41	0·28	0·23	0·46	0·42	0·37	0·40	0·37	0·31	0·46	0·48	0·45	0·29	0·45

	COM101	COM103	COM108	COM110	COM118	COM139	COM140	*PRA1*	*PRA74*	*PRA94*	*PRA301*	*PRA303*	*PRA306*
n:	>5	>5	>5	>5	>5	>5	>5						
Rock type:	H	H	H	H	H	H	H	*H*	*L*	*H*	*H*	*H*	*H*
SiO_2	0·03	0·03	0·04	0·04	0·04	0·04	0·05	*0·06*	*0·15*	*0·15*	*0·02*	*0·10*	*0·07*
TiO_2	0·10	0·12	0·09	0·20	0·18	0·25	0·16	*0·36*	*0·30*	*0·13*	*0·05*	*0·20*	*0·21*
Cr_2O_3	34·2	37·6	36·9	31·2	32·8	29·7	26·4	*29·3*	*17·2*	*35·1*	*29·6*	*40·3*	*20·6*
Al_2O_3	34·6	29·6	29·7	37·0	35·6	35·5	40·0	*39·5*	*50·5*	*33·3*	*39·5*	*28·4*	*46·8*
FeO	10·6	11·4	11·4	10·3	10·8	10·7	10·0	*10·0*	*8·4*	*10·9*	*9·1*	*10·4*	*9·4*
Fe_2O_3	2·95	4·08	5·52	3·27	2·62	5·83	4·29	*1·15*	*2·70*	*2·50*	*1·89*	*2·80*	*2·70*
MgO	17·6	16·4	16·6	18·0	17·5	17·5	18·3	*18·4*	*20·7*	*17·1*	*18·8*	*17·0*	*19·5*
MnO	0·12	0·13	0·13	0·12	0·11	0·13	0·11	*0·05*	*0·15*	*0·07*	*0·06*	*0·08*	*0·08*
NiO	0·20	0·19	0·22	0·26	0·20	0·26	0·27	*0·24*	*0·34*	*0·24*	*0·23*	*0·15*	*0·28*
Total	100·44	99·60	100·59	100·39	99·81	99·93	99·66	*99·06*	*100·44*	*99·49*	*99·25*	*99·43*	*99·64*
Mg#	0·72	0·66	0·64	0·71	0·70	0·66	0·70	*n.a.*	*n.a.*	*n.a.*	*n.a.*	*n.a.*	*n.a.*
Cr#	0·40	0·46	0·46	0·36	0·38	0·36	0·31	*0·33*	*0·19*	*0·41*	*0·33*	*0·49*	*0·23*

Samples in italic are from Bjerg *et al.* (2009); *n*, number of analyses; rock types as in Table 1; n.a., not available.

Nd and Sr. The compositions extend to highly radiogenic $^{176}Hf/^{177}Hf$ for a relatively narrow Nd (and Sr) isotope range (Fig. 8b and c). This variance has also been observed in samples from the present-day oceanic mantle (e.g. Hawaii: Bizimis *et al.*, 2003, 2007; Gakkel Ridge: Stracke *et al.*, 2011), and has been taken to suggest that Hf isotopes better retain a record of older depletion events than Nd and Sr isotopes in pyroxenes.

Re–Os isotopic composition

The Os isotopic results are given in Table 11. All bulk-rock Os isotopic compositions determined in this study are less radiogenic than primitive mantle estimates (Meisel *et al.*, 2001) and range from 0·1171 to 0·1257. Osmium isotopic ratios were recalculated to the average eruption age (EA) of the mantle xenoliths (10 Ma). These $^{187}Os/^{188}Os_{(EA)}$ ratios lead to γOs values between –1·0 and –7·8. Rhenium depletion ages (T_{RD} values; Walker *et al.*, 1989), calculated using the primitive mantle values of Meisel *et al.* (2001), yield early Paleozoic (0·5 Ga) to late Paleoproterozoic ages (1·7 Ga) for the stabilization of the SCLM below the North Patagonian Massif (Fig. 9). The $^{187}Re/^{188}Os$ compositions range from subchondritic (0·005) to suprachondritic (0·803). However, the majority of the samples yield $^{187}Re/^{188}Os$ ratios that are considerably lower than the chondritic estimate (0·40186; Shirey & Walker, 1998). Generally, the Os isotopic compositions do not correlate with $^{187}Re/^{188}Os$ (Fig. 10a) or indices of melt depletion, such as bulk-rock Al_2O_3 (Fig. 10b).

Highly siderophile element (HSE) concentrations

For the 18 samples chosen for Re–Os isotopic analysis platinum group element (PGE) and Re concentrations were also determined (Table 11). Rhenium contents range from 0·003 to 0·089 ppb. The scatter in Os concentrations is much higher, ranging from as low as 0·09 ppb (PD51) to 4·81 ppb (CH43). Sample CH43 is the only sample with an Os content higher than fertile mantle estimates (3·9 ppb; Becker *et al.*, 2006). The analyzed mantle xenoliths also exhibit variable contents of Ir (0·22–5·39 ppb), Ru (1·99–7·21 ppb), Pt (0·05–6·20 ppb) and Pd (0·002–2·710 ppb). On the basis of chondrite-normalized (CI) HSE patterns (Fig. 11a–c), three distinct groups can be recognized. Group I (Fig. 11a) is represented by samples with unfractionated iridium-group PGE (IPGE) and depleted palladium-group PGE (PPGE), consistent with melt extraction estimates (see below). However, all except sample CH63 are IPGE depleted with respect to the PM (Becker *et al.*, 2006). Group II samples exhibit a strong depletion in PPGE with a relative enrichment in Re (Fig. 11b). Two samples (CH1 and CH25) exhibit a pronounced Pd depletion. One sample

Table 8: Sulphide microprobe analyses

Sulphide phase:	Pn					Mss						
Sample:	PD51	COM103	COM139	PRA74	PRA306	COM103			COM139			
e/*i*:	*e*	*i*	*e*	*e*	*i*	*i*	*e*	*e*	*i*	*i*	*e*	*e*
Fe	31·9	28·4	28·4	29·5	31·4	29·0	49·7	38·6	45·3	36·8	37·7	39·5
Co	0·422	0·657	0·835	0·285	0·394	0·004	0·114	0·252	0·213	0·213	0·678	0·408
Ni	33·8	37·2	37·8	33·8	30·9	32·6	11·1	22·4	15·0	23·0	22·8	20·8
Cu	< 0·001	0·002	0·027	2·36	3·09	0·008	0·010	0·004	0·004	< 0·001	0·013	0·005
Cr	0·007	0·007	0·003	0·050	0·028	0·004	0·027	< 0·001	0·348	0·769	< 0·001	0·044
S	33·6	32·8	33·0	33·2	33·3	38·9	39·1	39·6	38·7	39·0	39·3	39·1
Total	99·74	99·06	100·13	99·20	99·05	100·52	100·09	100·81	99·62	99·83	100·45	99·88

Sulphide phase:	Mss									Cp	
Sample:	COM141	PRA74			PRA306					COM139	PRA306
e/*i*:	*e*	*e*	*e*	*i*	*e*	*e*	*e*	*e*	*e*	*e*	*e*
Fe	40·4	36·7	34·1	33·5	29·4	25·5	23·7	36·6	37·9	32·8	29·6
Co	0·357	0·246	0·291	0·186	0·331	0·327	0·313	0·311	0·330	0·007	0·015
Ni	20·90	24·50	27·50	26·50	28·50	40·40	40·50	24·10	22·90	0·68	0·38
Cu	0·281	0·372	0·093	0·031	0·164	0·151	1·409	0·262	0·192	30·9	33·5
Cr	0·018	0·020	0·004	0·122	0·075	0·052	0·046	0·064	0·055	0·004	0·054
S	37·6	38·4	38·3	37·8	41·6	33·7	33·3	38·4	37·8	34·8	34·7
Total	99·55	100·21	100·19	98·28	100·06	100·15	99·32	99·73	99·19	99·12	98·34

Sulphide phase:	Po		Hz		Bo	Cb	Py
Sample:	PD51	PRA306	PD51		PD51	PRA74	COM103
e/*i*:	*e*	*i*	*i*	*i*	*e*	*e*	*e*
Fe	62·6	58·6	2·5	2·1	15·3	37·8	43·1
Co	< 0·001	0·124	0·092	0·155	0·010	0·083	2·810
Ni	0·54	1·33	65·40	62·70	0·18	3·71	1·80
Cu	0·008	0·147	0·000	0·003	54·8	22·8	0·853
Cr	0·010	0·028	0·005	0·014	0·029	< 0·001	0·008
S	36·4	39·2	30·4	30·7	28·6	34·8	52·5
Total	99·61	99·49	98·38	95·68	99·07	99·18	101·00

Sulphide phase:	Laurite core*	Laurite rim*
Sample:	PD28	PD28
e/*i*:	*i*	*i*
Os	2·28	1·57
Ir	4·94	2·92
Ru	56·5	59·2
S	36·3	36·3
Total	100·0	100·0

e/*i*, enclosed/interstitial; Mss, monosulphide solid solution; Pn, pentlandite; Cp, chalcopyrite; Po, pyrrhotite; Hz, heazlewoodite; Bo, bornite; Cb, cubanite; Py, pyrite.
*Standardless microprobe EDS analyses of laurite.

(PRA301) deviates slightly from this group as it exhibits a positive Pt anomaly. Samples from Group III show a distinct Ir–Ru fractionation. Ruthenium exhibits a strong positive peak relative to Ir and Pt. One sample, PD64, slightly deviates from this group as its Os content is 2·66 ppb, much higher than those of the rest of Group III. Rhenium and in most cases also Pd are enriched relative to Pt (Fig. 11c). With the exception of sample PD64, HSE variation diagrams reveal a good correlation of Ir with Os in Group III (Fig. 12a). Ru is weakly correlated with Ir in Groups I and II, but yields higher Ru at given Ir concentrations in Group III (Fig. 12b). This suggests that in Groups I and II Ru and Ir might be controlled by the same mineral phases, whereas in Group III Ir and Os are probably hosted in the same phases. There is no obvious correlation of Re, Pt or Pd with Ir in any of the three groups (Fig. 12c–e).

DISCUSSION

Melt extraction estimates

With the exception of spinel–garnet-lherzolite PRA74, all the studied samples are harzburgites and appear to have have undergone extensive melt extraction, as recognizable in their bulk-rock major and trace element compositions (Table 2; Figs 4 and 5). The majority of the xenoliths contain clinopyroxenes with very low HREE abundances (Fig. 6). The only possible way to model these low REE abundances and still have clinopyroxene remaining in the residue is to use the melting model of

Bizimis *et al.* (2003) based on incremental melt removal, using clinopyroxene distribution coefficients from Norman (1998), source and melt modes from Kinzler (1997) and DMM values from Salters & Stracke (2004) as the starting source composition. Modeling of clinopyroxene trace element compositions after various degrees of melt extraction (Fig. 13) yields melting estimates for the Prahuaniyeu and Comallo spinel-

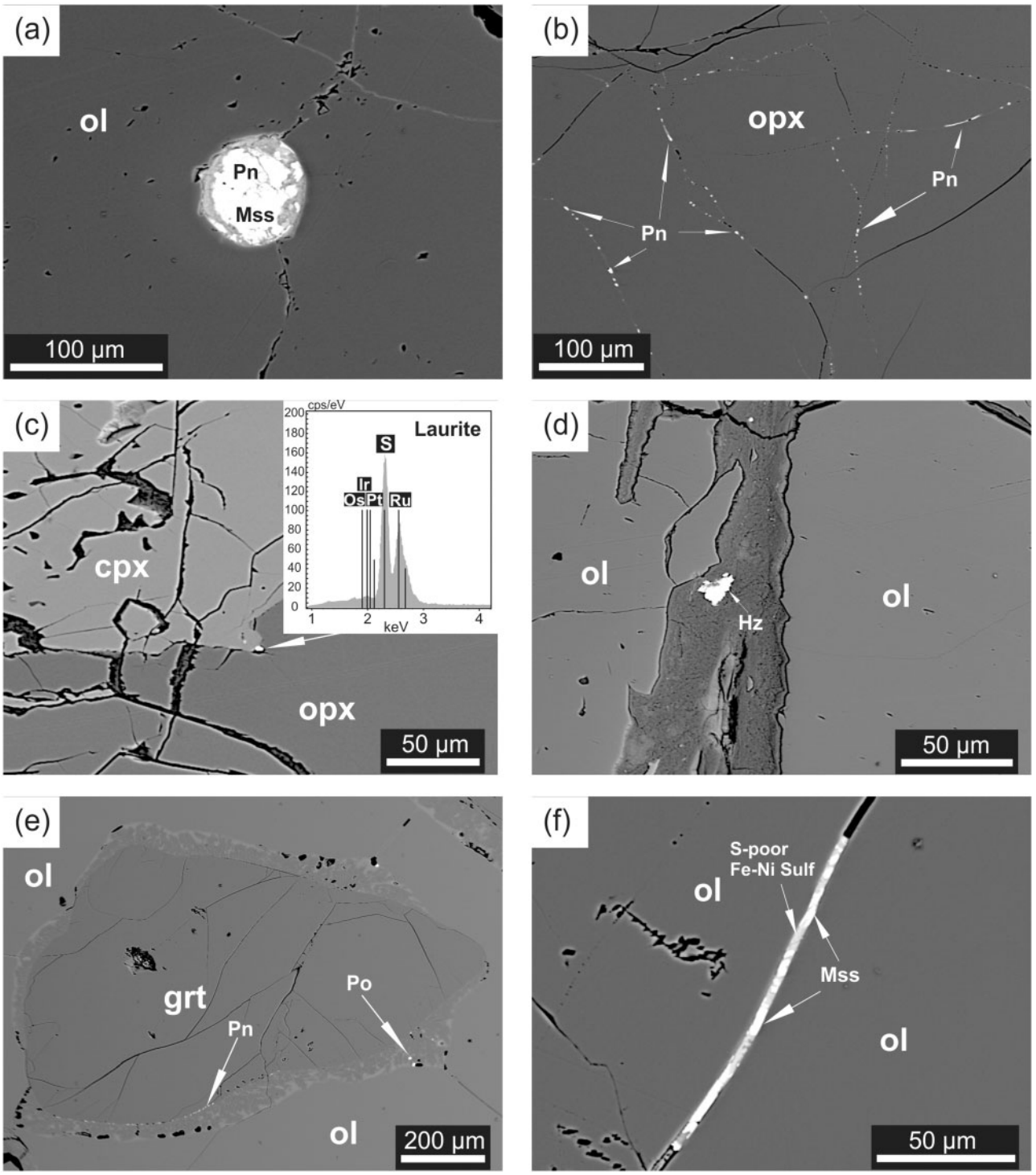

Fig. 7. Backscattered electron images of sulphide occurrences in the north Patagonian mantle xenoliths. (a) COM103: rounded sulphide inclusion in ol. Pn and Mss with light grey rim composed of altered, S-poor Fe–Ni phase. (b) COM108: sulphide (Pn) trails in orthopyroxene. (c) PD28: laurite at clinopyroxene–orthopyroxene grain boundary. Microprobe EDS peaks for platinum group elements shown in the inset. (d) PD51: sulphide (Hz) in devitrified glass vein. (e) PRA74: sulphides (Po and Pn) in symplectitic rim around garnet. (f) PRA306: intergranular sulphide between two olivine grains; Mss and S-poor Fe–Ni-phase. Mss, monosulphide solid solution; Pn, pentlandite; Po, pyrrhotite; Hz, heazlewoodite; ol, olivine; opx, orthopyroxene; cpx, clinopyroxene; grt, garnet.

harzburgites of up to 21% and 19% partial melting, respectively (see Table 12 and Fig. 14 for melt extraction estimates for all samples). The Cerro Chenque and Puesto Diaz mantle xenoliths have experienced up to 25% melt extraction. Samples PD1 and PD51 yield melting estimates of 'only' 12% and 5%, respectively. Modal compositions, however, suggest a similar depletion to the other PD samples. The modal compositions of samples PD1 and PD51 have 2·3% and 2·1% clinopyroxene, respectively, and are within the average range (2·3 mode %) of the Puesto Diaz samples (Table 1). Using bulk-rock major element compositions to model melt depletion (i.e. MgO vs Al_2O_3; Fig. 15) results in melt extraction estimates for the majority of the north Patagonian spinel-harzburgites, including all the Puesto Diaz samples, of between 20 and 30%. This is in good agreement with the partial melting estimates determined from the majority of the north Patagonian clinopyroxene trace elements. Hence, the differences within the sample suite are recognized only in trace element concentrations at similar bulk-rock and modal compositions.

Table 9: Estimated equilibrium T (and P) conditions after Brey & Köhler (1990)

	T (°C)	*P* (kbar)
sp-peridotites		
CH1	930	
CH12	789	
CH17	833	
CH25	748	
CH26	748	
CH42	946	
CH43	829	
CH63	767	
PD1	813	
PD7	800	
PD28	861	
PD32	830	
PD51	776	
PD61	882	
PD64	787	
COM101	905	
COM103	872	
COM108	875	
COM110	860	
COM118	911	
COM139	846	
COM140	878	
COM141	854	
COM142	867	
PRA1*	1061	
PRA94*	1160	
sp–grt-peridotite		
PRA74*	1192	22·4

Core temperature estimates of spinel-peridotites at an assumed pressure of 15 kbar.
*Bjerg *et al.* (2009).

Host basalt infiltration

All analyzed bulk-rock samples exhibit enrichment in highly incompatible elements, including the REE (Fig. 5). Primitive mantle-normalized bulk-rock REE patterns show elevated LREE abundances, even in those samples in which the clinopyroxene is not enriched in the LREE (clinopyroxene Group I, Fig. 6). No accessory minerals able to host highly incompatible elements were detected in those samples. Hence, these elements must be bound in interstitial phases. As these elements have not been incorporated in clinopyroxene, the enrichment process probably took place not too long before the transport of the xenoliths to the surface. Hence, interstitial host basalt glass is probably responsible for the bulk-rock enrichment of highly incompatible elements.

Metasomatism

Evidence from clinopyroxene and bulk-rock trace element compositions

It is obvious from the clinopyroxene and bulk-rock LREE enrichment in most of the north Patagonian xenolith samples that melt– or fluid–rock reaction processes have taken place. On the basis of their clinopyroxene

Table 10: Hf–Sr–Nd isotopic results

Sample	$^{176}Lu/^{177}Hf$	$^{176}Hf/^{177}Hf$	$2\sigma \times 10^{-7}$	εHf	T_{MA}	$^{87}Sr/^{86}Sr$	$2\sigma \times 10^{-7}$	$^{147}Sm/^{144}Nd$	$^{143}Nd/^{144}Nd$	$2\sigma \times 10^{-7}$	εNd	T_{MA}
CH1	0·1835	0·283854	9	37·8	0·4	0·703978	4	0·2189	0·512930	4	5·7	2·0
PD32	0·2605	0·287444	49	164·8	1·1	0·703945	21	0·1751	0·512761	4	2·4	–0·9
PD51	0·0598	0·283406	7	21·9	1·2	0·704835	4	0·2284	0·512871	4	4·5	1·1
COM103	0·0057	0·283179	4	13·9	–0·8	0·703588	4	0·1775	0·512939	4	5·9	–2·4
COM108	0·0060	0·283027	4	8·5	–0·5	0·703287	4	0·1471	0·512952	4	6·1	–1·0
COM139	0·0157	0·282992	4	7·3	–0·6	0·703399	3	0·1331	0·512923	4	5·6	–0·7
COM141	0·0102	0·283079	4	10·4	–0·7	0·703984	4	0·0886	0·512923	4	5·6	–0·4
PRA1	0·0328	0·283034	3	8·8	–27·0	0·703667	4	0·1702	0·512620	4	–0·3	0·1
PRA1	*n.d.*	*n.d.*		*n.d.*	*n.d.*	*n.d.*		*0·1693*	*0·512637*	*50*	*0·0*	*0·0*
PRA74 cpx	*n.d.*	*n.d.*		*n.d.*	*n.d.*	*n.d.*		*0·2146*	*0·513144*	*4*	*9·9*	*4·3*
PRA74 opx	*n.d.*	*n.d.*		*n.d.*	*n.d.*	*n.d.*		*0·3328*	*0·513145*	*47*	*9·9*	*0·6*
PRA74 grt	*n.d.*	*n.d.*		*n.d.*	*n.d.*	*n.d.*		*0·8259*	*0·513187*	*26*	*10·7*	*0·1*
PRA94	0·0373	0·283683	4	31·7	11·2	0·703886	3	0·1306	0·512726	3	1·7	–0·2
PRA301	0·7100	0·285390	24	92·1	0·2	0·702663	4	0·0501	0·513029	32	7·6	–0·4
PRA303	1·5558	0·285029	15	79·3	0·1	0·703820	5	0·0430	0·512660	11	0·4	0·0
COM-HB	*n.d.*	*n.d.*		*n.d.*	*n.d.*	*0·704390*		*n.d.*	*0·512740*		*n.d.*	*n.d.*

$^{176}Lu/^{177}Hf$ and $^{147}Sm/^{144}Nd$ were calculated using Lu and Hf and Sm and Nd concentrations of clinopyroxenes from LA-ICP-MS analyses (Table 6); εHf, εNd and T_{MA} for Hf and Nd calculated with reference to CHUR values $^{176}Lu/^{177}Hf = 0·0334$, $^{176}Hf/^{177}Hf = 0·282785$, $^{147}Sm/^{144}Nd = 0·1967$ and $^{143}Nd/^{144}Nd = 0·512638$ (Bouvier *et al.*, 2008). Samples in italic are from Bjerg *et al.* (2009) (PRA) and Ntaflos *et al.* (2000) (COM-HB). cpx, clinopyroxene; opx, orthopyroxene; grt, garnet; HB, host basalt.

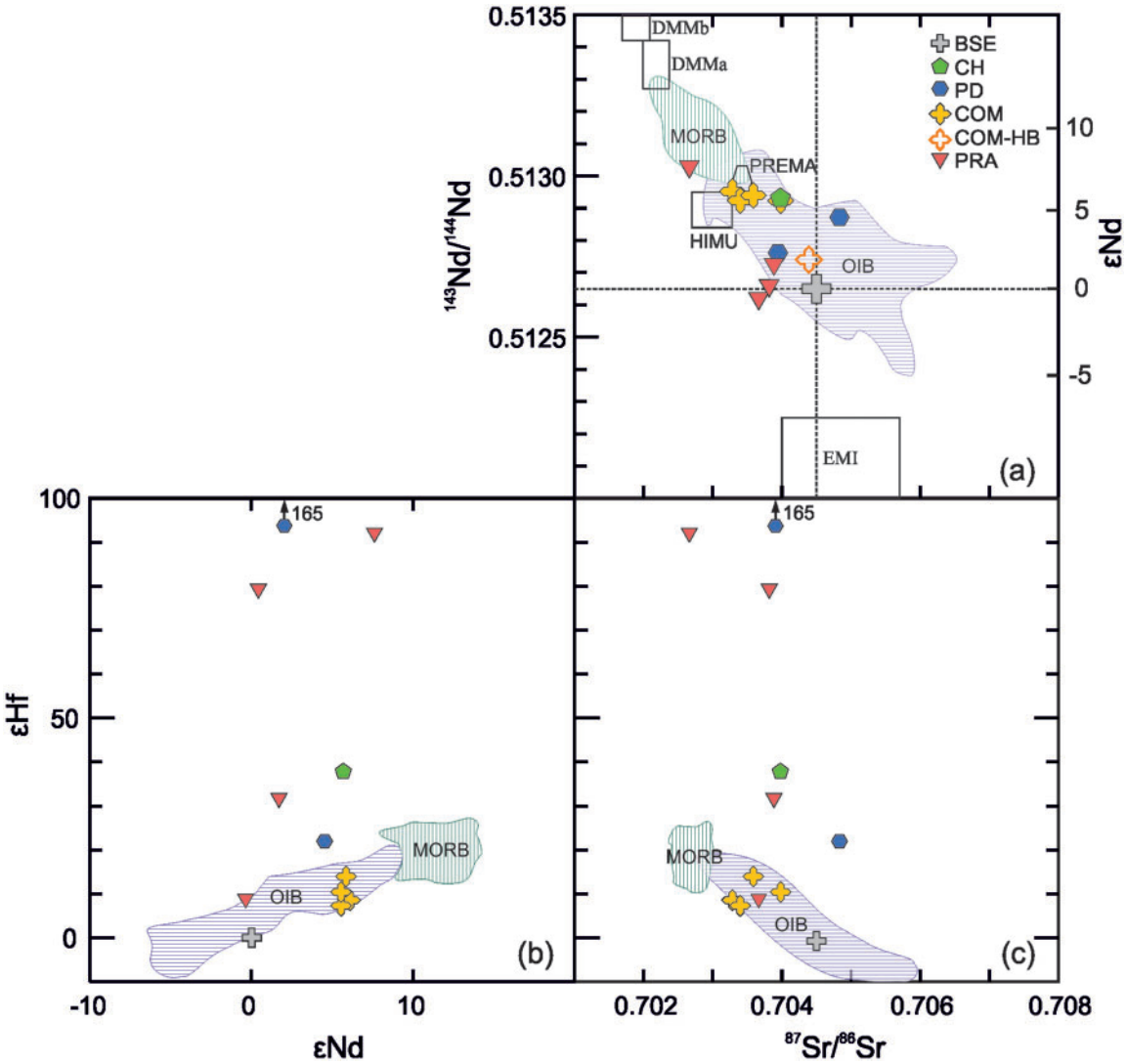

Fig. 8. Clinopyroxene $^{143}Nd/^{144}Nd$ vs $^{87}Sr/^{86}Sr$ (a), εHf vs εNd (b) and εHf vs $^{87}Sr/^{86}Sr$ (c). Fields in (a) for EMI, HIMU, PREMA and DMM from Zindler & Hart (1986); OIB and MORB fields from Hofmann (1997). Fields in (b) and (c) for MORB and OIB from Nowell *et al.* (1998). Abbreviations as in Fig. 1, BSE, Bulk Silicate Earth.

Table 11: Osmium isotopic results

Sample	Re (ppb)	Os (ppb)	Ir (ppb)	Ru (ppb)	Pt (ppb)	Pd (ppb)	$^{187}Re/^{188}Os$	$^{187}Os/^{188}Os_{(m)}$	$^{187}Os/^{188}Os_{(EA)}$	$2\sigma \times 10^{-6}$	γOs	T_{MA} (Ga)*	$T_{RD(EA)}$ (Ga)*
CH1	0·034	3·83	3·27	4·60	1·50	0·002	0·043	0·12573	0·12572	12	–1·0	0·6	0·5
CH25	0·026	3·76	2·02	3·72	0·48	0·003	0·033	0·12502	0·12501	4	–1·5	0·7	0·6
CH26	0·067	0·59	1·09	3·97	0·35	1·430	0·547	0·12525	0·12516	16	–1·4	–2·3	0·6
CH43	0·040	4·81	5·39	4·73	0·28	0·080	0·040	0·12410	0·12409	2	–2·3	0·8	0·8
CH63	0·024	3·82	3·02	7·21	4·65	1·050	0·030	0·12205	0·12204	18	–3·9	1·1	1·0
PD28	0·015	0·30	0·69	3·40	0·27	0·020	0·241	0·12371	0·12367	72	–2·6	1·8	0·8
PD32	0·009	2·90	2·07	3·12	3·93	0·580	0·015	0·12219	0·12219	6	–3·8	1·1	1·0
PD51	0·015	0·09	0·22	2·29	0·05	0·150	0·803	0·12373	0·12360	24	–2·6	–1·0	0·8
PD64	0·089	2·66	0·24	5·80	0·24	0·300	0·161	0·12472	0·12469	24	–1·8	1·1	0·7
COM103	0·008	0·54	1·25	3·65	1·47	0·030	0·071	0·12066	0·12065	14	–5·0	1·5	1·2
COM108	0·012	2·38	2·25	3·90	6·20	1·060	0·024	0·12038	0·12038	10	–5·2	1·3	1·3
COM139	0·026	2·04	3·08	5·09	1·31	0·170	0·061	0·12548	0·12547	4	–1·2	0·7	0·6
COM141	0·003	2·97	2·48	4·49	2·94	0·160	0·005	0·12395	0·12395	2	–2·4	0·8	0·8
PRA74	0·081	1·47	2·49	4·52	3·81	2·710	0·265	0·12429	0·12425	10	–2·1	1·9	0·7
PRA94	0·009	1·68	2·05	3·25	3·72	0·670	0·026	0·11708	0·11708	10	–7·8	1·8	1·7
PRA301	0·017	2·87	2·43	1·99	6·04	0·130	0·029	0·12446	0·12446	24	–2·0	0·8	0·7
PRA303	0·005	2·74	2·10	2·71	4·84	0·680	0·009	0·12522	0·12522	6	–1·4	0·6	0·6
PRA306	0·020	0·69	2·75	3·36	3·70	0·730	0·140	0·12325	0·12322	44	–2·9	1·3	0·9

*Re–Os model ages (T_{MA} and T_{RD}) were calculated using primitive upper mantle values from Meisel *et al.* (2001): $^{187}Re/^{188}Os = 0·4353$ and $^{187}Os/^{188}Os = 0·1296$, $\lambda^{187}Re = 1·666 \times 10^{-11}$ from Smoliar *et al.* (1996); $^{187}Os/^{188}Os_{(m)}$ is measured value, $^{187}Os/^{188}Os_{(EA)}$ is calculated value at time of eruption (10 Ma); $^{187}Re/^{188}Os$ determined using Re and Os concentrations. $T_{RD(EA)}$ is rhenium depletion age at time of eruption assuming Re = 0.

Table 12: Estimated melt extraction determined using clinopyroxene trace element compositions (Fig. 14)

sp-peridotites	%
CH1	12·0
CH12	22·0
CH17	25·0
CH25	12·0
CH26	21·0
CH42	22·0
CH43	24·0
CH63	21·0
PD1	12·0
PD27	23·5
PD28	21·5
PD32	22·0
PD51	5·0
PD61	15·0
PD64	20·5
COM103	7·5
COM108	12·0
COM118	6·5
COM139	11·0
COM140	5·0
COM141	19·0
COM142	7·0
PRA1	14·0
PRA94	13·5
PRA301	20·0
PRA303	21·5

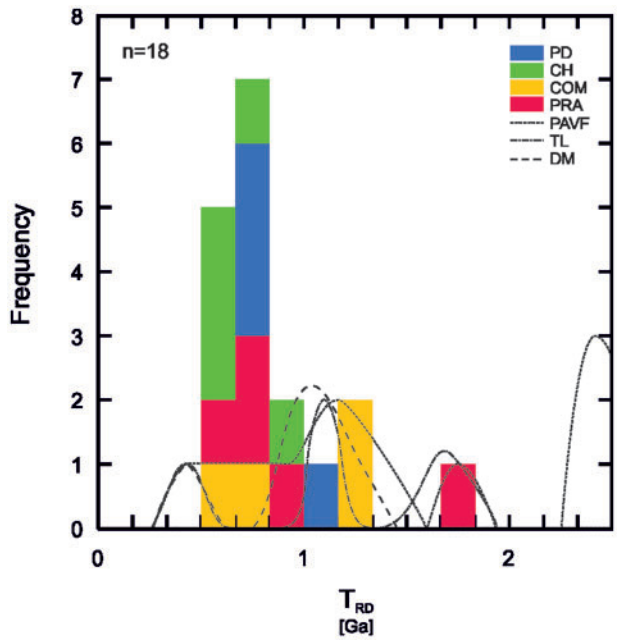

Fig. 9. T_{RD} for north Patagonian mantle xenoliths calculated using primitive mantle values from Meisel *et al.* (2001). For comparison the grey dashed lines represent south Patagonian mantle xenoliths from Mundl *et al.* (2015). Abbreviations as in Fig. 2; PAVF, Pali Aike Volcanic Field; TL, Tres Lagos; DM, Deseado Massif.

trace element compositions, most of the studied samples indicate melt(s) percolating through the peridotites. Ionov *et al.* (2002a), after Vernières *et al.* (1997), attributed variable trace element enrichment patterns of clinopyroxenes to chromatographic effects during

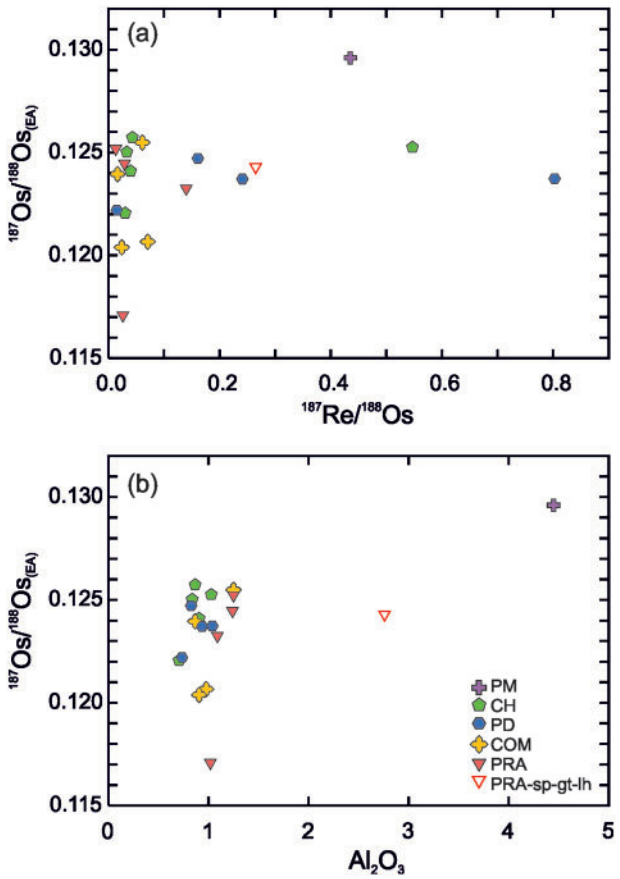

Fig. 10. (a) $^{187}Os/^{188}Os_{(EA)}$ vs $^{187}Re/^{188}Os$ and (b) $^{187}Os/^{188}Os_{(EA)}$ vs bulk-rock Al_2O_3. $^{187}Os/^{188}Os_{(EA)}$ is calculated value at time of eruption (10 Ma). Abbreviations as in Fig. 2; PM values from Meisel *et al.* (2001): $^{187}Re/^{188}Os = 0·4353$ and $^{187}Os/^{188}Os = 0·1296$, and McDonough & Sun (1995): $Al_2O_3 = 4.45$ wt.%.

reactive porous melt flow. Progressive percolation of a melt through the mantle can be illustrated by looking at four mantle xenolith samples from Puesto Diaz that reflect different stages of reaction with an advancing percolating melt (Fig. 16). As melt rises within a magma conduit it infiltrates the surrounding wall-rocks. Consequently, this melt, probably strongly enriched in LREE > MREE > HREE, reacts with the harzburgite through which it percolates and changes its composition. This reaction within the studied samples is mainly reflected in the clinopyroxene trace element compositions and to a far lesser extent by major elements. None of the samples have been modally altered. Hence, this melt percolation affected the composition of the already existing minerals, especially clinopyroxene, but did not form a new generation of silicate minerals. The Al_2O_3 and TiO_2 contents in clinopyroxene are slightly higher in samples PD1 (3·45 wt % and 0·30 wt %, respectively) and PD51 (3·96 wt % and 0·64 wt %, respectively) compared with the average Al_2O_3 and TiO_2 contents of the Puesto Diaz harzburgites (2·74 wt % and 0·12 wt %, respectively) (Table 5). The Mg# values of clinopyroxene and orthopyroxene, as well as the Fo content of olivine in samples PD1 and PD51, do not differ from those of the rest of the sample suite and,

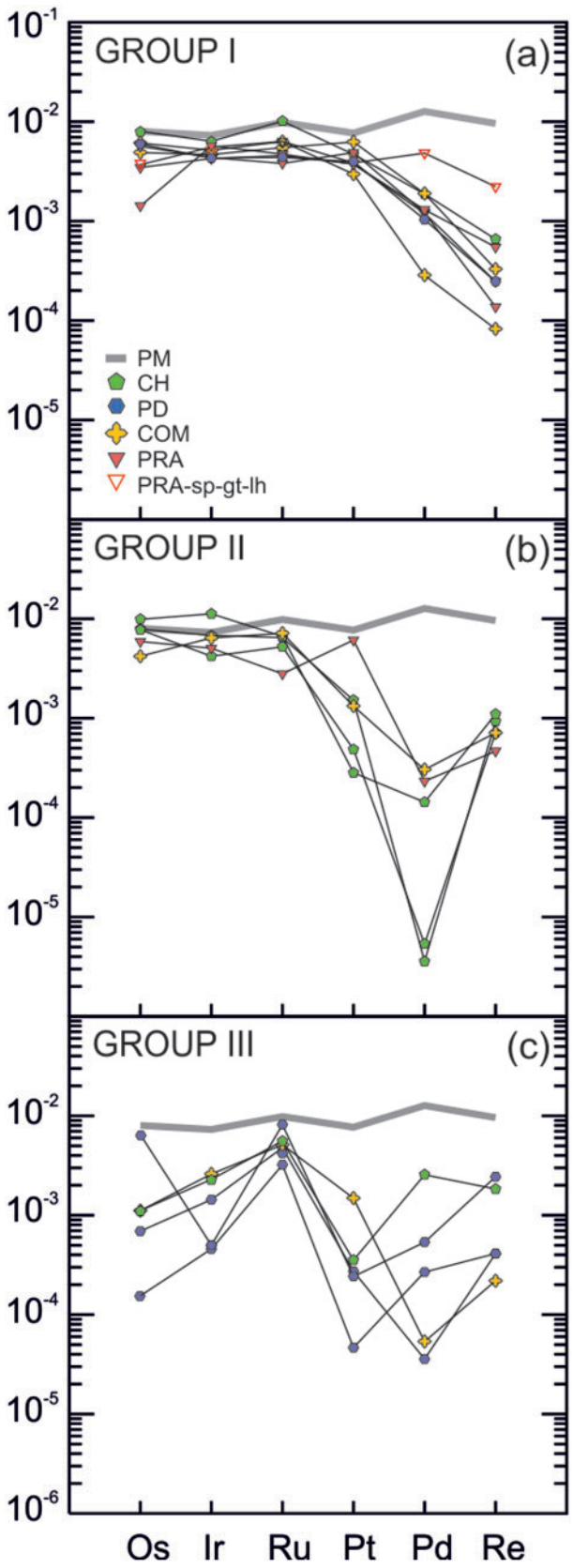

Fig. 11. Chondrite-normalized highly siderophile element patterns. Three groups can be distinguished (see text for explanation). Normalization values (CI) from Anders & Grevesse (1989). Wide grey line represents the primitive mantle of Becker *et al.* (2006).

hence, have not been affected by the percolating melt. On the other hand, samples PD1 and PD51 exhibit slightly lower cr# in spinel (0·32 and 0·23, respectively) relative to the average cr# in PD spinels (0·38). This suggests that interaction of spinel with a percolating melt caused an increase in Al_2O_3 in spinel, which consequently lowered its cr#. It is obvious from major element compositions of its constituent minerals that sample PD51 was affected most by this percolating melt, followed by sample PD1. Samples PD64 and PD32, interpreted to be furthest away from a melt conduit, have not been affected in terms of major elements. Trace element compositions show a continuous reaction with the harzburgites as the melt propagates through the rocks. As mentioned above, the melt is assumed to be enriched in LREE, MREE and to a lesser extent in HREE. Reaction with this percolating melt results in refertilization of the harzburgite closest to the melt conduit. This is reflected in PM-normalized clinopyroxene REE patterns that exhibit enriched HREE < MREE > LREE (Fig. 16, I). As the melt reacts with the harzburgite closest to the melt conduit it subsequently changes its composition as a result of chromatographic fractionation of the melt (e.g. Navon & Stolper, 1987; Takazawa *et al.*, 1992). This 'new' melt then continues to propagate intergranularly through the mantle section further away from the melt conduit where it again reacts with the next section of rock (Fig. 16, II). The PM-normalized REE patterns in Fig. 16, I and II, are characterized by a small enrichment in HREE and a hump in the MREE suggesting that while melt, probably enriched in HREE < MREE and more so in LREE, percolated through this mantle section, the HREE and MREE were incorporated into clinopyroxene whereas the LREE, the more incompatible elements, largely remained in the melt. This LREE-enriched and HREE-depleted melt then advanced through the mantle and probably reacted with a different mantle section further along its path, resulting in peridotites showing stronger LREE than MREE enrichment (Fig. 16, III). The last stage of reaction is represented by sample PD32, in which the LREE are strongly enriched. The budget of MREE in the melt at this stage is nearly exhausted and hence enrichment in the harzburgite PD32 is minor (Fig. 16, IV). We suggest that samples closest to melt conduits have experienced the strongest refertilization in terms of their trace element compositions. Our model calculations for melt extraction estimates (Fig. 14) suggest that sample PD51 has experienced 'only' 5% partial melting. However, its bulk-rock and mineral major element and modal proportions reflect a much stronger depletion. Hence, addition of the HREE to clinopyroxene by percolating melts after the initial melt depletion can result in misleading clinopyroxene-based melt extraction estimates.

Sr–Nd–Hf isotope systematics and implications for metasomatism

In a plot of $^{143}Nd/^{144}Nd$ vs $^{87}Sr/^{86}Sr$ (Fig. 8a) all spinel-harzburgites from COM, CH and PD plot within the

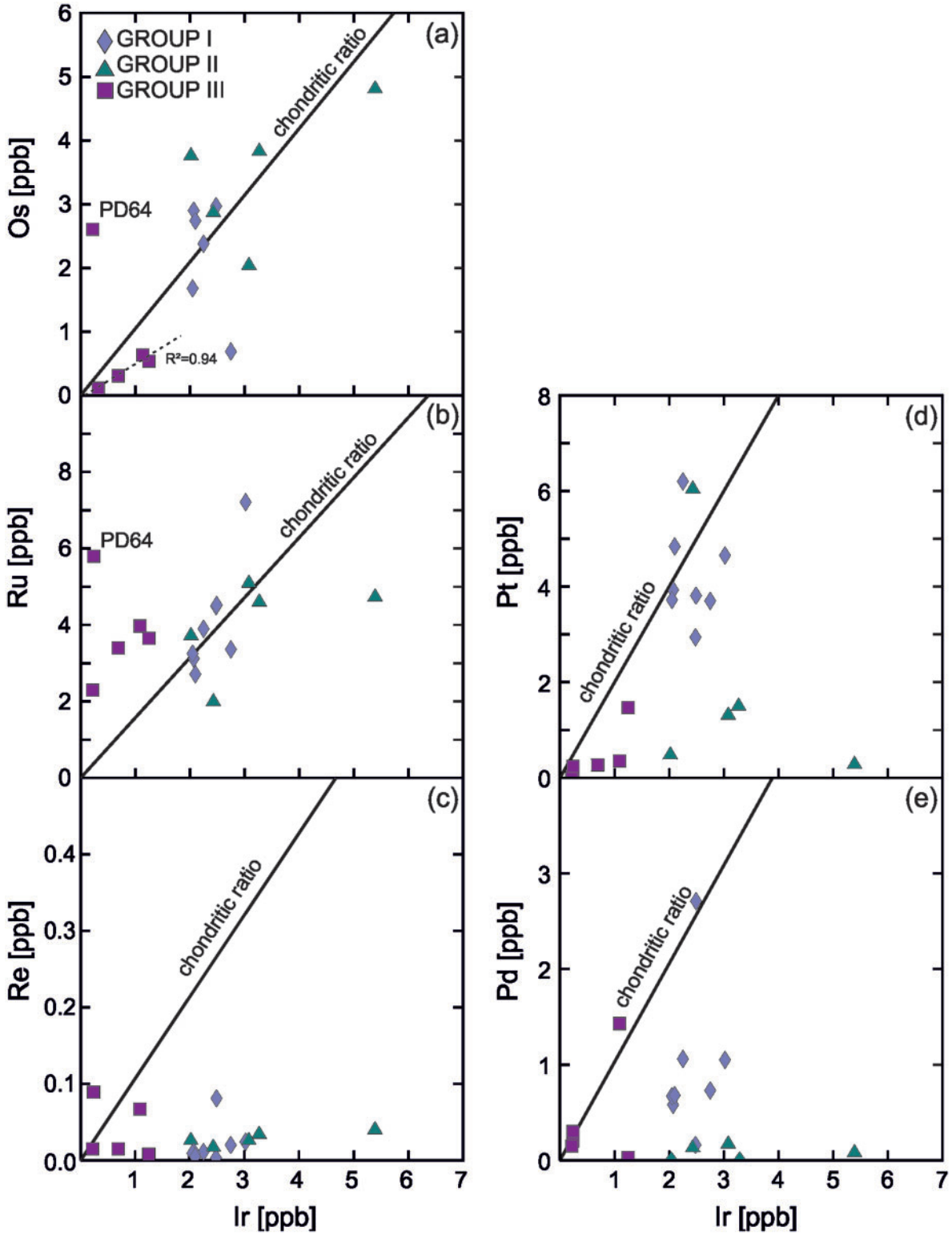

Fig. 12. Bivariate HSE concentration plots for the north Patagonian mantle xenoliths. Three groups are distinguished according to their CI-normalized HSE patterns (Fig. 11). (a) Good correlation of Os and Ir contents in Group III samples; (b) Groups I and II show good correlation of Ru with Ir; Group III samples have higher Ru at a given Ir content; (c–e) no correlation of Re, Pt or Pd with Ir.

ocean island basalt (OIB) field (Hoffmann, 1997). One sample from Prahuaniyeu (PRA301) plots beyond the OIB field, in the MORB field, whereas the other three PRA samples have less radiogenic Nd and more radiogenic Sr and plot just outside or on the edge of the OIB field. All four COM samples yield very homogeneous present-day εNd values between+5·6 and+6·1. In contrast, Sr isotope ratios vary between 0·703287 and

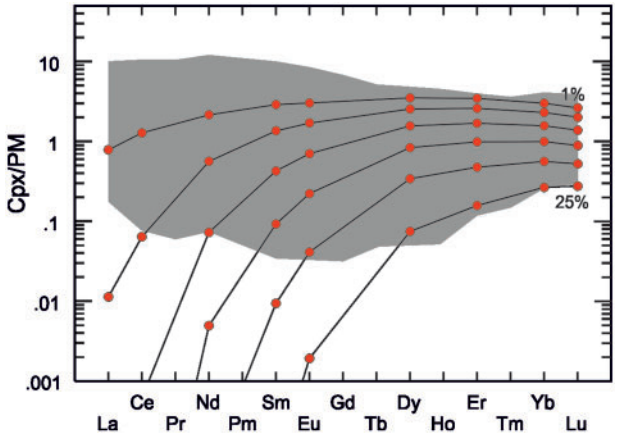

Fig. 13. Partial melting degrees modeled using the method of Bizimis *et al.* (2003), mineral–melt distribution coefficients from Norman (1998), source modes and melt modes from Kinzler (1997), DMM (Salters & Stracke, 2004) as the starting source. Orange circles: PM-normalized clinopyroxene REE patterns after 1%, 5%, 10%, 15%, 20% and 25% melt extraction, respectively. Grey field represents north Patagonian mantle xenoliths from this study. All samples exhibit extensive metasomatic enrichment of LREE and MREE relative to the strong depletion expected for these elements after large amounts of melt extraction.

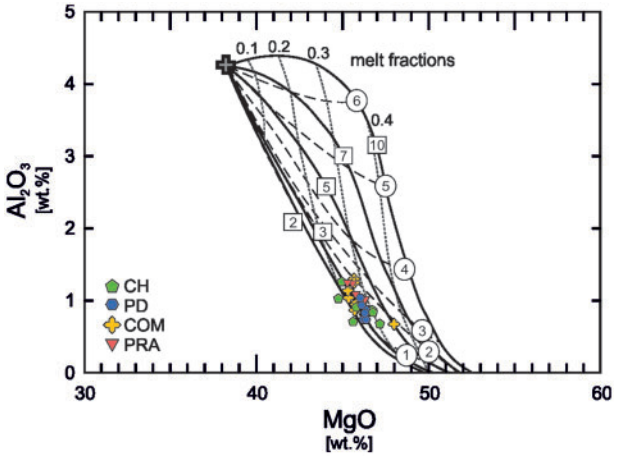

Fig. 15. Fractional melting estimates using the bulk-rock Al_2O_3 vs MgO model of Herzberg (2004). The majority of the north Patagonian spinel-harzburgites plot between 20 and 30% melt extraction at final melting pressures between 1 and 2 GPa. dotted lines represent different melt fractions; bold lines labelled with numbers in squares are initial melting pressures (GPa); dashed lines labelled with circled numbers represent final melting pressures (GPa). Abbreviations as in Fig. 2; starting composition from Herzberg (2004).

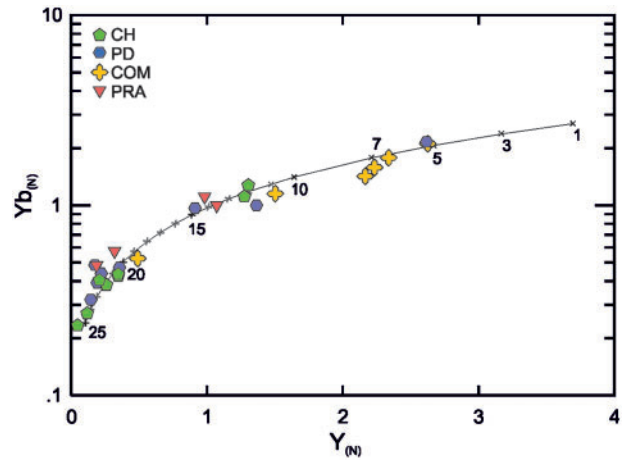

Fig. 14. Clinopyroxene PM-normalized (N) Yb vs PM-normalized Y for north Patagonian mantle xenoliths from this study. Line indicates melt increments modeled using the method of Bizimis *et al.* (2003). Parameters used for modeling are as in Fig. 13. Crosses with numbers indicate degrees of partial melting (1–25%); grey crosses represent 1% melting steps. Abbreviations as in Fig. 2.

0·703984 in the same four samples. This weak decoupling of Sr isotopes from Nd isotopes can be attributed to metasomatism by slab-derived fluid or melt as these commonly have high $^{87}Sr/^{86}Sr$ and moderate $^{143}Nd/^{144}Nd$ (e.g. Zanetti *et al.*, 1999). A second way in which to decouple Sr from Nd isotopes in mantle xenoliths involves melt percolation processes (Ionov *et al.*, 2002b; Conceição *et al.*, 2005), which have been observed in our samples. The above-cited researchers argued for a decoupling of Sr from Nd isotopes owing to the 'chromatographic effect' of a percolating melt rather than reaction of a peridotite protolith with high $^{87}Sr/^{86}Sr$ subduction-related melts as proposed in the first model. However, in the mantle samples studied from the Comallo area subduction-related metasomatism can be considered likely as Comallo is located only ~300 km away from the subduction front. Also, the majority of samples from COM are modally metasomatized mantle peridotites comprising high abundances of amphibole and/or phlogopite, whose existence can probably be attributed to subduction-related fluid–rock interaction (Ntaflos *et al.*, 2000; Papadopoulou *et al.*, 2014).

Hf isotopic compositions vary strongly within the studied sample suite, with εHf values ranging from +7 to +165. Whereas all COM samples plot within the Nd–Hf mantle array (Fig. 8b), samples from PD, CH and PRA have highly radiogenic $^{176}Hf/^{177}Hf$ leading to εHf values of up to +165 and plot above the fields for OIB and MORB. These samples define an almost vertical trend in Fig. 8b and c and show strong decoupling of Hf from Nd and Sr isotopic compositions. Highly radiogenic Hf isotope ratios could reflect ancient melt depletion of the mantle section, whereas decoupled $^{143}Nd/^{144}Nd$ and $^{87}Sr/^{86}Sr$ provide evidence for metasomatic disturbance of the samples. All harzburgites plotting within the OIB field (Fig. 8b and c) yield future Hf T_{MA} ages. These future T_{MA} ages of samples from COM and PRA1 suggest a recent disturbance of the Lu–Hf system. This disturbance is also reflected in very low $^{176}Lu/^{177}Hf$ ratios resulting from elevated Hf concentrations in COM clinopyroxene (Table 6). Hf concentrations are very low in samples PRA301 and PRA303 (Table 6), as expected for samples that have experienced high degrees of melt extraction. However, despite their high εHf values of

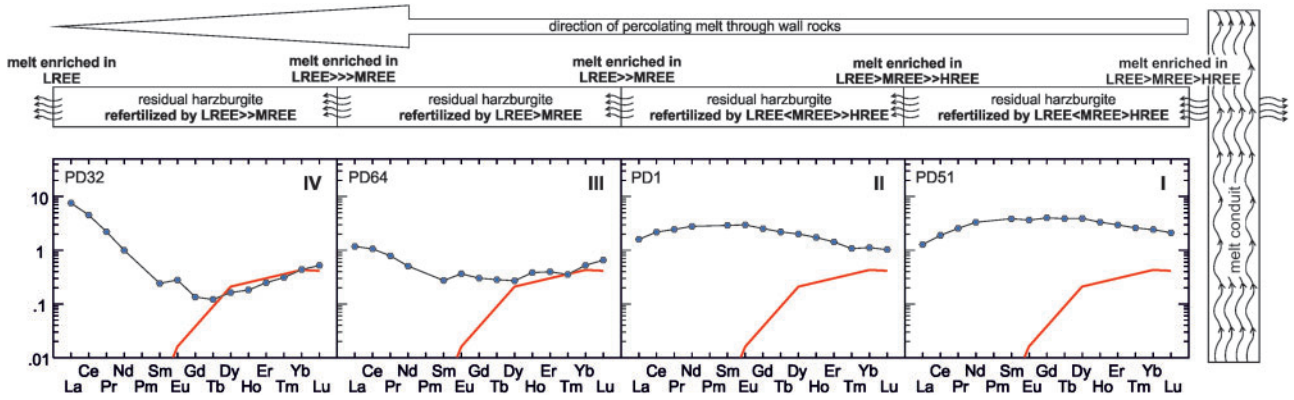

Fig. 16. Schematic representation of the percolating melt model, similar to that of Ionov *et al.* (2002a). Melt infiltrates horizontally from a nearby melt conduit. I, II, III, IV are the clinopyroxene PM-normalized REE patterns of Puesto Diaz samples PD51, PD1, PD64 and PD32, respectively. Red line represents the modeled clinopyroxene composition after 22% melt extraction, using the same parameters as in Fig. 13. Melt advances from right to left and changes its composition as it reacts with each mantle section (from I to IV).

+92 and +79, respectively, and hence high $^{176}Hf/^{177}Hf$ ratios, calculated model ages yield very young T_{MA} ages of 80–210 Ma. This suggests that the Lu–Hf system in these samples has been significantly disturbed, as T_{RD} ages calculated from Os isotopic compositions suggest an initial melt extraction event at least 1·7 Gyr ago. The oldest Hf T_{MA} values for north Patagonian mantle xenoliths have been determined in samples from Puesto Diaz. Sample PD51 yields the oldest T_{MA} (1·25 Ga) of the entire sample suite. From the trace element composition of clinopyroxene, we have suggested that this sample was severely affected by melt percolation processes and as a consequence was refertilized in terms of trace elements. Hence, the Lu–Hf system has been disturbed significantly. Sample PD32 yields a T_{MA} of 1·09 Ga. However, this age is distinctly younger than the suggested ages for the initial basement formation of the North Patagonian Massif (1·7–2·1 Ga; Martínez Dopico *et al.*, 2011).

Metasomatic processes inferred from HSE compositions

Many researchers have studied the effects of melt percolation processes on highly siderophile elements (e.g. Büchl *et al.*, 2002; Lorand *et al.*, 2004, 2010; Ackerman *et al.*, 2009; Wang *et al.*, 2009). In mantle rocks, the HSE reside mainly in base metal sulphides (Alard *et al.*, 2000; Luguet *et al.*, 2001) and HSE-bearing alloys (Luguet *et al.*, 2007; Lorand *et al.*, 2008, 2010, 2013; Ackerman *et al.*, 2013). At high degrees of partial melting (>20%) these base metal sulphides should be fully consumed in the melt (Luguet *et al.*, 2003). This results in strong depletion of the residual mantle in Pd and Re (and partially in Pt) as these elements are more incompatible relative to the IPGE (Os, Ir, Ru) (Pearson *et al.*, 2004). The remaining HSE Os, Ir and Ru (and Pt) are subsequently redistributed into microphases, such as minerals of the laurite (RuS_2)–erlichmanite (OsS_2) series and Pt–Ir–Os and/or Ru–Ir–Os alloys (Luguet *et al.*, 2007; Lorand *et al.*, 2010; Fonseca *et al.*, 2012). Melting degree estimates for our north Patagonian harzburgites inferred from clinopyroxene trace element and bulk-rock major element compositions suggest between 20 and 30% of melt extraction. Hence, the compatible HSE are expected to reside in such microphases. However, as these minerals are rare and very small in mantle xenoliths, they are difficult to detect. In one sample, PD28, laurite was identified using energy-dispersive spectroscopy (EDS) peaks (Fig. 7c, right upper corner). A standardless microprobe EDS analysis revealed no significant Os or Ir concentrations in the laurite (Table 8). Hence, these elements are probably hosted by (Pt)–Ir–Os alloys. A lack of correlation of Ir and Ru in HSE Group III samples (Fig. 12b) also suggests that these elements do not reside in the same phases. With the exception of sample PD64, all other harzburgites from Group III show a good correlation of Os with Ir (Fig. 12a). This indicates that these elements are hosted by the same phases (i.e. Pt–Ir–Os alloys).

Information from bulk-rock and clinopyroxene trace element concentrations suggests at least one metasomatic event in which melts percolated through the mantle section sampled by some of our studied xenoliths. Owing to the multi-stage magmatic history of northern Patagonia since the Precambrian, as noted above in the section on geological setting, several melt–rock reaction processes could have probably taken place in the underlying subcontinental lithospheric mantle. The PGE patterns of samples from Group III exhibit strong fractionation of Ru from Os, Ir and the PPGE. This fractionation cannot be due to melting processes, but rather results from percolating melts removing phases that host Os, Ir and probably Pt. Whereas laurite remains in the mantle section affected by melt percolation, Pt–Ir–Os alloys must have been physically removed as a result of this process. Lorand *et al.* (2004) suggested that IPGE can behave incompatibly during melt percolation at high melt/rock ratios. They also proposed that Pt–Ir–Os alloys may be stripped or dissolved by a silicate melt flowing through a mantle section (Lorand *et al.*,

2004, 2010). Why laurite remains in the peridotite and is not dissolved or removed from it like the Pt–Ir–Os alloys remains uncertain. Brenan & Andrews (2001) suggested that laurite has a high temperature stability. However, this high temperature stability also applies to IPGE-rich alloys and hence cannot be responsible for fractionation of Ru from Ir, Os and Pt. One explanation could be that the percolating melt was S-saturated and hence picked up Os, Ir and Pt residing as alloys, but left laurite, a Ru-sulphide, behind. Our proposed scenario therefore suggests that under certain conditions, laurite can be more stable during melt percolation processes than Pt–Ir–Os alloys.

Generally, most of our studied samples from HSE Groups I and II exhibit a slight deficit in compatible HSE, which is evidenced by low IPGE concentrations relative to primitive mantle values (Becker *et al.*, 2006) (Fig. 11). This can also be attributed to melt percolation processes removing some of the primary sulphides and hence decreasing the abundance of Os, Ir and Ru at high melt/rock ratios (e.g. Becker *et al.*, 2001; Büchl *et al.*, 2002; Lorand *et al.*, 2003). Percolating melts probably are responsible for the precipitation of secondary sulphides. Minor amounts of base metal sulphides have been found in most north Patagonian mantle xenoliths. As they should be completely consumed during extensive partial melt extraction (>20%) (Luguet *et al.*, 2003), their existence in our highly depleted samples, predominantly on or close to grain boundaries, hints at their addition from a percolating melt. Elevated Re and in some cases also Pd contents support this assumption. Whether the removal of Pt–Ir–Os alloys and the precipitation of secondary sulphides from the percolating melt was a single event or if these processes took place separately cannot be answered at this time. Elevated Re concentrations could also be the result of host basalt infiltration and hence late-stage enrichment in Re. The mantle xenolith carrying host basalts erupted between 1 and 25 Myr ago. An enrichment in Re from host basalt infiltration, therefore, would not have affected the Os isotopic compositions, as the decay of Re to radiogenic Os is much too slow to elevate significantly the $^{187}Os/^{188}Os$. A combination of suprachondritic $^{187}Re/^{188}Os$ and subchondritic $^{187}Os/^{188}Os$ in two north Patagonian samples (CH26 and PD51) suggests that the addition of Re must have taken place rather recently.

Timing of the stabilization of the SCLM underneath the North Patagonian Massif

The $^{187}Os/^{188}Os$ ratios of our studied sample suite are comparable with those of off-cratonic mantle samples (Pearson *et al.*, 2002; Reisberg *et al.*, 2005; and references therein) and are much higher than those reported for Archean cratonic peridotites (Pearson *et al.*, 1995*a*, 1995*b*; Carlson *et al.*, 1999). As noted above, Os isotopic ratios do not correlate with either $^{187}Re/^{188}Os$ or indices of melt depletion such as bulk-rock Al_2O_3 (Fig. 10). This indicates a disturbance of the Re–Os system in the majority of the studied north Patagonian mantle xenoliths after the initial melting event, which is in agreement with our proposed theory of melt percolation affecting the HSE systematics, which in turn affects the Os isotopic data. An important fact to keep in mind is that after the melt percolation event that removed most of Os residing in Pt–Ir–Os alloys (HSE Group III), the concentration of Os was significantly lowered. Hence, the production of ^{187}Os from Re introduced into the rocks by the percolating melt easily elevates the $^{187}Os/^{188}Os$ ratio, resulting in much younger T_{RD} values than expected and, in some cases, in suprachondritic $^{187}Re/^{188}Os$ ratios. Rhenium depletion model ages (T_{RD}) calculated using primitive mantle values (Meisel *et al.*, 2001) yield a late Paleoproterozoic formation age of the SCLM underneath the North Patagonian Massif. However, our oldest calculated T_{RD} (1·7 Ga; PRA94) is clearly younger than the oldest model ages (T_{MA}) determined by Schilling *et al.* (2008), who suggested an at least early Paleoproterozoic (2·1 Ga) stabilization of the SCLM underneath Prahuaniyeu. Sample PRA74 yields a T_{RD} of only 0·7 Ga. However, because this spinel–garnet-lherzolite is fertile and hence most of the Re remained in the sample after the initial melting event, this age must be considered an absolute minimum. In contrast to T_{RD}, Re–Os model age (T_{MA}) calculations also include the analyzed $^{187}Re/^{188}Os$ ratios and assume that this ratio is representative of the long-term history of the mantle, hence that it has not been affected by Re or Os alteration processes (Shirey & Walker, 1998). From the HSE systematics and the bulk-rock and mineral compositions, we can assume that sample PRA74 has not been affected by metasomatic processes or significant host basalt infiltration that altered the Re/Os ratio. Therefore, the calculated 1·9 Ga T_{MA} (Table 11) can be considered reasonable. This T_{MA} is still younger than but similar to the suggested formation age of 2·1 Ga for the oldest North Patagonian Massif basement rocks (Martínez Dopico *et al.*, 2011). The COM mantle xenoliths suggest SCLM stabilization in that area around 1·3 Ga. The oldest determined T_{RD} of samples from Puesto Diaz and Cerro Chenque indicate formation of the SCLM at least 1·0 Gyr ago. This is in good agreement with the T_{MA} determined from the Hf isotopic composition of clinopyroxene from Puesto Diaz sample PD32 (1·1 Ga). This sample is interpreted not to have been affected by percolating melts in terms of clinopyroxene Hf concentrations. Also, Re–Os and HSE systematics reveal no obvious disturbance in this sample. Hence, the calculated Os T_{RD} of 1·0 Ga, as well as the Hf T_{MA} of 1·1 Ga, may provide a good estimate for the timing of the stabilization of the SCLM below Puesto Diaz.

Implications for more than one SCLM fragment beneath the North Patagonian Massif

Bulk-rock and mineral major and trace element compositions (Tables 2–7) reveal the strongly depleted nature of the entire studied sample suite. However, it is

important to note that the four PRA spinel-harzburgites were specifically chosen for isotopic analyses from a large sample suite studied by Bjerg *et al.* (2009) because of their refractory character, which allows the comparison of their isotopic compositions with those from the highly depleted COM, PD and CH samples. Generally, the Prahuaniyeu sample suite from Bjerg *et al.* (2009) is represented by mantle xenoliths ranging from fertile lherzolites to highly depleted harzburgites (Fig. 4). This clearly distinguishes Prahuaniyeu from the sample suites of Puesto Diaz and Cerro Chenque. All the PD and CH samples are spinel-harzburgites, and hence the SCLM underneath Puesto Diaz and Cerro Chenque appears to be strongly depleted in basaltic components. A lack of fertile samples from Puesto Diaz and Cerro Chenque could be attributed to biased sampling methods. However, the large number (>100) of mantle xenoliths collected from these localities confirms the strongly depleted character of the SCLM. Therefore, our samples can be considered representative.

Furthermore, the Re–Os isotopic systematics suggest SCLM formation beneath Prahuaniyeu at least 1·7 Gyr ago. This is in good agreement with a reported T_{RD} of 1·7 Ga for the oldest PRA sample from Schilling *et al.* (2008). Mantle xenoliths from Puesto Diaz and Cerro Chenque yield oldest T_{RD} values of 1·0 Ga, significantly younger than the PRA xenoliths.

The obvious disparities in the character of the mantle samples (range of fertility and age) from Prahuaniyeu and Puesto Diaz–Cerro Chenque suggest different origins and evolutionary histories. This could imply that the SCLM beneath the North Patagonian Massif may consist of at least two separate mantle domains.

CONCLUSIONS

The majority of the north Patagonian mantle xenoliths analyzed in this study have experienced extensive melt extraction of between 20 and 30%. This is reflected in the very low HREE concentrations of clinopyroxene, as well as in their bulk-rock compositions. The fact that the majority of the xenoliths are highly depleted spinel-harzburgites clearly distinguishes them from south Patagonian mantle xenoliths. In contrast, samples from southern Patagonia cover a wide range from fertile lherzolites to strongly depleted harzburgites and dunites.

All the studied north Patagonian mantle xenoliths have experienced cryptic metasomatism resulting in refertilization of the samples. We suggest that an advancing percolating melt reacted with a highly depleted harzburgite protolith as it propagated through the wall-rocks of local melt conduits and subsequently changed its composition. This reaction of a chromatographically fractionated melt with mantle rocks at various stages is evidenced by enriched bulk-rock and clinopyroxene trace element abundances of different degrees. However, these melt–rock reactions have overall not affected bulk-rock major element or modal contents. Disturbed isotopic and HSE compositions confirm that metasomatic processes have taken place. Trace element contents, HSE systematics and Os–Hf–Nd–Sr isotopic data suggest melt percolation processes and commonly host basalt infiltration to have affected the SCLM underneath north Patagonia.

The oldest T_{RD} (1·7 Ga) and T_{MA} (1·9 Ga) determined from the Os isotopic composition of samples PRA94 and PRA74, respectively, suggest stabilization of the SCLM underneath northern Patagonia by at least late Paleoproterozoic times. The oldest calculated T_{RD} from Comallo and Puesto Diaz–Cerro Chenque is 1·3 Ga and 1·0 Ga, respectively, indicating younger stabilization ages for the SCLM underneath these regions. However, the HSE concentrations of most north Patagonian mantle xenoliths have been significantly modified by metasomatic processes, and hence most samples are not suitable for determining the timing of SCLM formation. Thus, the majority of T_{RD} ages obtained in this study must be considered minima.

FUNDING

This study was financed by the FWF grant P 23557-N19 (PI: Th. Ntaflos). L.A. acknowledges the Scientific Programme CEZ: RVO67985831 of the Institute of Geology, Academy of Sciences of the Czech Republic (Os isotopic and PGE analyses). M.B. acknowledges support from award NSF-EAR-1347890 (Hf isotopic analyses).

ACKNOWLEDGEMENTS

We gratefully acknowledge Peter Nagl (University of Vienna) for his help with XRF analyses. We thank Vojtech Erban (Czech Geological Survey) for Os isotope analyses, and Jana Ďurišová (Czech Academy of Sciences) for the ICP-MS analyses of highly siderophile elements. We are grateful to Martha Papadopoulou for conducting some of the Comallo microprobe analyses. We especially want to thank Suzanne Kay, Michel Grégoire and Charles Stern for their constructive reviews, and Marjorie Wilson for the editorial handling.

REFERENCES

Ackerman, L., Walker, R. J., Puchtel, I. S., Pitcher, L., Jelínek, E. & Strnad, L. (2009). Effects of melt percolation on highly siderophile elements and Os isotopes in subcontinental lithospheric mantle: A study of the upper mantle profile beneath Central Europe. *Geochimica et Cosmochimica Acta* **73**, 2400–2414.

Ackerman, L., Pitcher, L., Strnad, L., Puchtel, I. S., Jelínek, E., Walker, R. J. & Rohovec, J. (2013). Highly siderophile element geochemistry of peridotites and pyroxenites from Horní Bory, Bohemian Massif: Implications for HSE behavior in subduction-related upper mantle. *Geochimica et Cosmochimica Acta* **100**, 158–175.

Alard, O., Griffin, W. L., Lorand, J.-P., Jackson, S. E. & O'Reilly, S. Y. (2000). Non-chondritic distribution of the highly siderophile elements in mantle sulfides. *Nature* **407**, 891–894.

Anders, E. & Grevesse, N. (1989). Abundances of the elements: Meteoritic and solar. *Geochimica et Cosmochimica Acta* **59**, 197–214.

Ardolino, A., Franchi, M., Remersal, M. & Salani, F. (1999). El volcanismo en la Patagonia Extraandina. In: Haller, M. J. (ed.) *Geología Argentina. Anales SEGEMAR* **29**, 579–612.

Becker, H., Shirey, S. B. & Carslon, R. W. (2001). Effects of melt percolation on the Re–Os systematics of peridotite from a Paleozoic convergent plate margin. *Earth and Planetary Science Letters* **188**, 107–121.

Becker, H., Horan, M. F., Walker, R. J., Gao, S., Lorand, J.-P. & Rudnick, R. L. (2006). Highly siderophile element composition of the Earth's primitive upper mantle: Constraints from new data on peridotite massifs and xenoliths. *Geochimica et Cosmochimica Acta* **70**, 4528–4550.

Birck, J. L., Roy Barman, M. & Capmas, F. (1997). Re–Os isotopic measurements at the femtomole level in natural samples. *Journal of Geostandards and Geoanalysis* **20**, 19–27.

Bizimis, M., Sen, G. & Salters, V. J. M. (2003). Hf–Nd isotope decoupling in the oceanic lithosphere: constraints from spinel peridotite from Oahu, Hawaii. *Earth and Planetary Science Letters* **217**, 43–58.

Bizimis, M., Griselin, M., Lassiter, J. C., Salters, V. J. M. & Sen, G. (2007). Ancient recycled mantle lithosphere in the Hawaiian plume: osmium–hafnium isotopic evidence from peridotite mantle xenoliths. *Earth and Planetary Science Letters* **257**, 259–273.

Bizimis, M., Salters, V. J. M., Garcia, M. O. & Norman, M. D. (2013). The composition and distribution of rejuvenated component across the Hawaiian plume: Hf–Nd–Sr–Pb isotope systematics of Kuala lavas and pyroxenite xenoliths. *Geochemistry, Geophysics, Geosystems* **14**, 4458–4478.

Bjerg, E. A., Ntaflos, T., Kurat, G., Dobosi, G. & Labudía, C. H. (2005). The upper mantle beneath Patagonia, Argentina, documented by xenoliths from alkali basalts. *Journal of South American Earth Sciences* **18**, 125–145.

Bjerg, E. A., Ntaflos, T., Thöni, M., Aliani, P. & Labudia, C. H. (2009). Heterogeneous lithospheric mantle beneath northern Patagonia: evidence from Prahuaniyeu garnet- and spinel-peridotites. *Journal of Petrology* **50**, 1267–1298.

Bouvier, A., Vervoort, J. D. & Patchett, P. J. (2008). The Lu–Hf and Sm–Nd isotopic composition of CHUR: constraints from unequilibrated chondrites and implications for the bulk composition of terrestrial planets. *Earth and Planetary Science Letters* **273**, 48–57.

Brenan, J. M. & Andrews, D. (2001). High-temperature stability of laurite and Ru–Os–Ir alloy and their role in PGE fractionation in mafic magmas. *Canadian Mineralogist* **39**, 341–360.

Brey, G. P. & Köhler, T. (1990). Geothermobarometry in four-phase lherzolites II. New thermobarometers and practical assessment of existing thermobarometers. *Journal of Petrology* **31**, 1353–1378.

Büchl, A., Brügmann, G. E., Muenker, C. & Hofmann, A. W. (2002). Melt percolation monitored by Os-isotopes and PGE abundances: a case study from the mantle section of the Troodos ophiolite. *Earth and Planetary Science Letters* **204**, 385–402.

Carlson, R. W., Pearson, D. G., Boyd, F. R., Shirey, S. B., Irvine, G., Menzies, A. H. & Gurney, J. J. (1999). Re–Os systematics of lithospheric peridotites: Implications for lithosphere formation and preservation. In: Gurney, J. J., Gurney, J. L., Pascoe, M. D. & Richardson, S. H. (eds) *Proceedings of the 7th International Kimberlite Conference*. Cape Town: Red Roof Design, pp. 99–108.

Cohen, A. S. & Waters, F. G. (1996). Separation of osmium from geological materials by solvent extraction for analysis by thermal ionization mass spectrometry. *Analytica Chimica Acta* **332**, 269–275.

Conceição, R. V., Mallmann, G., Koester, E., Schilling, M., Bertotto, G. W. & Rodriguez-Vargas, A. (2005). Andean subduction-related mantle xenoliths: Isotopic evidence of Sr–Nd decoupling during metasomatism. *Lithos* **82**, 273–287.

Creaser, R. A., Papanastassiou, D. A. & Wasserburg, G. J. (1991). Negative thermal ion mass spectrometry of osmium, rhenium, and iridium. *Geochimica et Cosmochimica Acta* **55**, 397–401.

Fonseca, R. O. C., Laurenz, V., Mallmann, G., Luguet, A., Hoehne, N. & Jochum, K. P. (2012). New constraints on the genesis and long term stability of Os-rich alloys in the Earth's mantle. *Geochimica et Cosmochimica Acta* **87**, 227–242.

Gorring, M. L. & Kay, S. M. (2000). Carbonatite metasomatized peridotite xenoliths from southern Patagonia: implications for lithospheric processes and Neogene plateau magmatism. *Contributions to Mineralogy and Petrology* **140**, 55–72.

Herzberg, C. (2004). Geodynamic information in peridotite petrology. *Journal of Petrology* **45**, 2507–2530.

Hofmann, A. W. (1997). Mantle geochemistry: the message from oceanic volcanism. *Nature* **385**, 219–229.

Ionov, D. A., Bodinier, J.-L., Mukasa, S. B. & Zanetti, A. (2002a). Mechanisms and sources of mantle metasomatism: major and trace element compositions of peridotite xenoliths from Spitsbergen in the context of theoretical modeling. *Journal of Petrology* **43**, 2219–2259.

Ionov, D. A., Mukasa, S. B. & Bodinier, J.-L. (2002b). Sr–Nd–Pb isotopic compositions of peridotite xenoliths from Spitsbergen: numerical modeling indicates Sr–Nd decoupling in the mantle by melt percolation metasomatism. *Journal of Petrology* **43**, 2261–2278.

Kay, S. M., Ramos, V. A., Mpodozis, C. & Sruoga, P. (1989). Late Paleozoic to Jurassic silicic magmatism at the Gondwana margin: analogy to the Middle Proterozoic in North America? *Geology* **17**, 324–328.

Kay, S. M., Ardolino, A. A., Gorring, M. L. & Ramos, V. A. (2007). The Somuncura Large Igneous Province in Patagonia: interaction of a transient mantle thermal anomaly with a subducting slab. *Journal of Petrology* **48**, 53–77.

Kempton, P. D., Hawkesworth, C. J., Lopez-Escobar, L., Pearson, D. G. & Ware, A. G. (1999a). Spinel ± garnet lherzolite xenoliths from Pali Aike, Part 2: trace element and isotopic evidence on the evolution of lithospheric mantle beneath southern Patagonia. In: Gurney, J. J., Gurney, J. L., Pascoe, M. D. & Richardson, S. H. (eds) *T. J. B. Dawson Volume, Proceedings of the 7th International Kimberlite Conference*. Cape Town: Red Roof Design, pp. 415–428.

Kempton, P. D., Hawkesworth, C. J., Lopez-Escobar, L., Pearson, D. G. & Ware, A. G. (1999b). Spinel ± garnet lherzolite xenoliths from Pali Aike, Part 1: Petrography, mineral chemistry and geothermobarometry. In: Gurney, J. J., Gurney, J. L., Pascoe, M. D. & Richardson, S. H. (eds) *T. J. B. Dawson Volume, Proceedings of the 7th International Kimberlite Conference*. Cape Town: Red Roof Design, pp. 415–428.

Kinzler, R. J. (1997). Melting of mantle peridotite at pressures approaching the spinel to garnet transition: application to mid-ocean ridge basalt petrogenesis. *Journal of Geophysical Research* **102**, 853–874.

Labudía, C. H., Bjerg, E. A. & Ntaflos, T. (2011). Nuevas dataciones del vulcanismo del noroeste de la Meseta de Somoncurá, Argentina. In: Leanza, H., Franchini, M., Impiccini, A., Pettinari, G., Sigismondi, M., Pons, J. & Tunik,

M. (eds) *Proceedings XVIII Congreso Geológico Argentino (CD), Neuquén*, Argentina, pp. 356–357.

Lorand, J. P. (1990). Are spinel lherzolite xenoliths representative of abundance of sulfur in the upper mantle? *Geochimica et Cosmochimica Acta* **54**, 1487–1492.

Lorand, J.-P., Reisberg, L. & Bedini, L. M. (2003). Platinum-group elements and melt percolation processes in Sidamo spinel peridotite xenoliths, Ethiopia, East African Rift. *Chemical Geology* **196**, 58–75.

Lorand, J.-P., Delpech, G., Grégoire, M., Moine, B., O'Reilly, S. Y. & Cottin, J.-Y. (2004). Platinum-group elements and the multistage metasomatic history of Kerguelen lithospheric mantle, South Indian Ocean. *Chemical Geology* **208**, 195–214.

Lorand, J.-P., Luguet, A., Alard, O., Bezos, A. & Meisel, T. (2008). Abundance and distribution of platinum-group elements in orogenic lherzolites; a case study in a Fontete Rouge lherzolite (French Pyrénées). *Chemical Geology* **248**, 174–194.

Lorand, J.-P., Alard, O. & Luguet, A. (2010). Platinum-group element micronuggets and refertilization process in the Lherz peridotite. *Earth and Planetary Science Letters* **289**, 298–310.

Lorand, J.-P., Luguet, A. & Alard, O. (2013). Platinum-group element systematics and petrogenetic processing of the continental upper mantle: A review. *Lithos* **164–167**, 2–21.

Luguet, A., Alard, O., Lorand, J.-P., Pearson, N. J, Ryan, C. G. & O'Reilly, S. Y. (2001). LAM-ICPMS unravel the highly siderophile element geochemistry of abyssal peridotites. *Earth and Planetary Science Letters* **189**, 285–294.

Luguet, A., Lorand, J.-P. & Seyler, M. (2003). Sulfide petrology and highly siderophile element geochemistry of abyssal peridotites: a coupled study of samples from the Kane Fracture Zone (45°W, 23°20N, MARK area, Mid-Atlantic ridge). *Geochimica et Cosmochimica Acta* **67**, 1553–1570.

Luguet, A., Shirey, S., Lorand, J.-P., Horan, M. F. & Carlson, R. C. (2007). Residual platinum group minerals from highly depleted harzburgites of the Lherz massif (France) and their role in HSE fractionation of the mantle. *Geochimica et Cosmochimica Acta* **71**, 3082–3097.

Mallick, S., Standish, J. J. & Bizimis, M. (2015). Constraints on the mantle mineralogy of an ultra-slow ridge: Hafnium isotopes in abyssal peridotites and basalts from the 9–25°E Southwest Indian Ridge. *Earth and Planetary Science Letters* **410**, 42–53.

Martínez Dopico, C. I., López de Luchi, M. G., Rapalini, A. E. & Kleinhanns, I. C. (2011). Crustal segments in the North Patagonian Massif, Patagonia: An integrated perspective based on Sm–Nd isotope systematics. *Journal of South American Earth Sciences* **31**, 324–341.

McDonough, W. F. & Sun, S. (1995). The composition of the Earth. *Chemical Geology* **120**, 223–253.

Meisel, T., Walker, R. J., Irving, A. J. & Lorand, J.-P. (2001). Osmium isotopic compositions of mantle xenoliths: A global perspective. *Geochimica et Cosmochimica Acta* **65**, 1311–1323.

Mundl, A., Ntaflos, T., Ackerman, L., Bizimis, M., Bjerg, E. A. & Hauzenberger, C. A. (2015). Meso- and Paleoproterozoic subcontinental lithospheric mantle domains beneath southern Patagonia: Isotopic evidence for its connection to Africa and Antarctica. *Geology* **43**, 39–42.

Munker, C., Weyer, S., Scherer, E. & Mezger, K. (2001). Separation of high field strength elements (Nb, Ta, Zr, Hf) and Lu from rock samples for MC-ICPMS measurements. *Geochemistry, Geophysics, Geosystems* **2** paper number 10.1029/2001GC000183.

Munoz, J., Troncoso, R., Duhart, P., Crignola, P., Rarmer, L. & Stern, C. R. (2002). The relation of the mid-Tertiary coastal magmatic belt in south–central Chile to the late Oligocene increase in plate convergence rate. *Revista Geologica de Chile* **27**, 177–204.

Navon, O. & Stolper, E. (1987). Geochemical consequences of melt percolation—the upper mantle as a chromatographic column. *Journal of Geology* **95**, 285–307.

Ntaflos, T., Günther, M., Labudia, H. C., Bjerg, E. A., Kurat, G. & Dingeldey, C. (2000). Isotopic and geochemical evolution of the Cenozoic basalts from Rio Negro, Patagonia, Argentina. In: *31st International Geological Congress, Rio de Janeiro, Extended Abstract #SD603s* (electronic version).

Ntaflos, T., Bjerg, E. A., Labudía, C. H. & Kurat, G. (2007). Depleted lithosphere from the mantle wedge beneath Tres Lagos, southern Patagonia, Argentina. *Lithos* **94**, 46–65.

Norman, M. D. (1998). Melting and metasomatism in the continental lithosphere: laser ablation ICPMS analysis of minerals in spinel lherzolites from eastern Australia. *Contributions to Mineralogy and Petrology* **130**, 240–255.

Nowell, G. M., Kempton, P. D., Noble, S. R., Fitton, J. G., Saunders, A. D., Mahoney, J. J. & Taylor, R. N. (1998). High precision Hf isotope measurements of MORB and OIB by thermal ionization mass spectrometry: insights into the depleted mantle. *Chemical Geology* **149**, 211–233.

Pankhurst, R. J. & Rapela, C. R. (1995). Production of Jurassic rhyolite by anatexis of the lower crust of Patagonia. *Earth and Planetary Science Letters* **134**, 23–36.

Pankhurst, R. J., Rapela, C. W., Fanning, C. M. & Márquez, M. (2006). Gondwanide continental collision and the origin of Patagonia. *Earth-Science Reviews* **76**, 235–257.

Papadopoulou, M., Ntaflos, T., Bjerg, E. A. & Grégoire, M. (2014). Hydrous metasomatism and melt percolation in the lithospheric mantle wedge underneath Comallo, Rio Negro, Argentina. *EGU 2014 Conference Abstracts* EGU2014–11111.

Pearce, N. J. G., Perkins, Westgate, J. A., Gorton, M. P., Jackson, S. E., Neal, C. R. & Chenery, S. P. (1997). A compilation of new and published major and trace element data for NIST SRM 610 and NIST SRM 612 glass reference materials. *Geostandards Newsletter* **21**, 115–144.

Pearson, D. G., Carlson, R. W., Shirey, S. B., Boyd, F. R. & Nixon, P. H. (1995a). The stabilization of Archaean lithospheric mantle: a Re–Os isotope study of peridotite xenoliths from the Kaapvaal craton. *Earth and Planetary Science Letters* **134**, 341–357.

Pearson, D. G., Carlson, R. W., Shirey, S. B., Boyd, F. R., Pokhilenko, N. P. & Shimizu, N. (1995b). Re–Os, Sm–Nd and Rb–Sr isotope evidence for thick Archaean lithospheric mantle beneath the Siberia craton modified by multi-stage metasomatism. *Geochimica et Cosmochimica Acta* **59**, 959–977.

Pearson, D. G., Irvine, G. J., Carlson, R. W., Kopylova, M. G. & Ionov, D. A. (2002). The development of lithospheric keels beneath the earliest continents: time constraints using PGE and Re–Os systematics. In: Fowler, C. M. R., Ebinger, C. J. & Hawkesworth, C. J. (eds) *The Early Earth: Physical, Chemical and Biological Development. Geological Society, London, Special Publications* **199**, 65–90.

Pearson, D. G., Irvine, G. J., Ionov, D. A., Boyd, F. R. & Dreibus, G. E. (2004). Re–Os isotope systematics and platinum group element fractionation during mantle melt extraction: a study of massif and xenolith peridotite suites. *Chemical Geology* **208**, 29–59.

Ramos, V. A. (1999). Plate tectonic setting of the Andean Cordillera. *Episodes* **22**, 183–190.

Ramos, V. A. (2008). Patagonia: A Paleozoic continent adrift? *Journal of South American Earth Sciences* **26**, 235–251.

Rapalini, A., López de Luchi, M., Martínez Dopico, C., Lince Klinger, F., Giménez, M. & Martínez, P. (2010). Did Patagonia

collide with Gondwana in the Late Paleozoic? Some insights from a multidisciplinary study of magmatic units of the North Patagonian Massif. *Geológica Acta* **8**, 349–371.

Rapalini, A., López de Luchi, M., Tohver, E. & Cawood, P. A. (2013). The South American ancestry of the North Patagonian Massif: geochronological evidence for an autochthonous origin? *Terra Nova* **25**, 337–342.

Rapela, C. W. & Kay, S. M. (1988). Late Paleozoic to Recent magmatic evolution of northern Patagonia. *Episodes* **11**, 175–182.

Rapela, C. W., Spalletti, L. A., Merodio, J. C. & Aragón, E. (1988). Temporal evolution and spatial variation of early Tertiary volcanism in the Patagonian Andes (40°S–42°30′S). *Journal of South American Earth Sciences* **1**, 75–88.

Reisberg, L., Zhi, X., Lorand, J.-P., Wagner, C., Peng, Z. & Zimmermann, C. (2005). Re–Os and S systematics of spinel peridotite xenoliths from east central China: Evidence for contrasting effects of melt percolation. *Earth and Planetary Science Letters* **239**, 286–308.

Rivalenti, G., Mazzucchelli, M., Laurora, A., Ciuffi, S. I. A., Zanetti, A., Vannucci, R. & Cingolani, C. A. (2004). The back-arc mantle lithosphere in Patagonia, South America. *Journal of South American Sciences* **17**, 121–152.

Salters, V. J. M. & Stracke, A. (2004). Composition of the depleted mantle. *Geochemistry, Geophysics, Geosystems* **5** doi:10.1029/2003GC000597.

Schilling, M., Conceição, R. V., Mallmann, G., Koester, E., Kawashita, K., Hervé, F., Morata, D. & Motoki, A. (2005). Spinel-facies mantle xenoliths from Cerro Redondo, Argentina Patagonia: Petrographic, geochemical, and isotopic evidence of interaction between xenoliths and host basalt. *Lithos* **82**, 485–502.

Schilling, M. E., Carlson, R. W., Conceição, R. V., Dantas, C., Bertotto, G. W. & Koester, E. (2008). Re–Os isotope constraints on subcontinental lithospheric mantle evolution of southern South America. *Earth and Planetary Science Letters* **268**, 89–101.

Shirey, S. B. & Walker, R. J. (1995). Carius tube digestion for low blank rhenium–osmium analysis. *Analytical Chemistry* **67**, 2136–2141.

Shirey, S. B. & Walker, R. J. (1998). The Re–Os isotope system in cosmochemistry and high-temperature geochemistry. *Annual Review of Earth and Planetary Sciences* **26**, 423–500.

Skewes, M. A. & Stern, C. R. (1979). Petrology and geochemistry of alkali basalts and ultramafic inclusions from the Palei-Aike volcanic field in southern Chile and the origin of the Patagonian plateau lavas. *Journal of Volcanology and Geothermal Research* **6**, 3–25.

Smoliar, M. I., Walker, R. J. & Morgan, J. W. (1996). Re–Os ages of Group IIA, IIIA, IVA and IVB iron meteorites. *Science* **271**, 1099–1102.

Stern, C. R., Saul, S., Skewes, M. A. & Futa, K. (1989). Garnet peridotite xenoliths from the Pali-Aike alkali basalts of southernmost South America. In: Rossi, J. (ed.) *Kimberlites and Related Rocks. Geological Society of Australia Special Publication* **14**, 735–744.

Stern, C. R., Kilian, R., Olker, B., Hauri, E. H. & Kyser, T. K. (1999). Evidence from mantle xenoliths for relatively thin (<100 km) continental lithosphere below the Phanerozoic crust of southernmost South America. *Lithos* **48**, 217–235.

Stracke, A., Snow, J. E., Hellebrand, E., von der Handt, A., Bourdon, B., Kirbaum, K. & Günther, D. (2011). Abyssal peridotite Hf isotopes identify extreme mantle depletion. *Earth and Planetary Science Letters* **308**, 359–368.

Takazawa, E., Frey, F. A., Shimizu, N., Obata, M. & Bodinier, J. L. (1992). Geochemical evidence for melt migration and reaction in the upper mantle. *Nature* **359**, 55–58.

Vernières, J., Godard, M. & Bodinier, J.-L. (1997). A plate model for the simulation of trace element fractionation during partial melting and magma transport in the Earth's upper mantle. *Journal of Geophysical Research* **102**, 24771–24784.

Völkening, J., Walczyk, T. & Heumann, K. G. (1991). Osmium isotope ratio determinations by negative thermal ionization mass spectrometry. *International Journal of Mass Spectrometry and Ion Processes* **105**, 147–159.

Walker, R. J., Carlson, R. W., Shirey, S. B. & Boyd, F. R. (1989). Os, Sr, Nd, and Pb isotope systematics of southern African peridotite xenoliths: Implications for the chemical evolution of subcontinental mantle. *Geochimica et Cosmochimica Acta* **53**, 1583–1595.

Wang, J., Hattori, K. H., Li, J. & Stern, C. R. (2008). Oxidation state of Paleozoic subcontinental lithospheric mantle below the Pali Aike volcanic field in southernmost Patagonia. *Lithos* **105**, 98–110.

Wang, K.-L., O'Reilly, S. Y., Griffin, W. L., Pearson, N. J. & Zhang, M. (2009). Sulphides in mantle peridotites from Penghu Islands, Taiwan: melt percolation, PGE fractionation, and the lithospheric evolution of the South China block. *Geochimica et Cosmochimica Acta* **73**, 4531–4557.

Zanetti, A., Mazzucchelli, M., Rivalenti, G. & Vannucci, R. (1999). The Finero phlogopite-peridotite massif: an example of subduction-related metasomatism. *Contributions to Mineralogy and Petrology* **134**, 107–122.

Zindler, A. & Hart, S. (1986). Chemical geodynamics. *Annual Review of Earth and Planetary Sciences* **14**, 493–571.